

# High-resolution Simulation of Upper-Ocean Submesoscale Eddies in the Kuroshio Extension: Energy Budget

Haijin Cao,<sup>a,b</sup> Baylor Fox-Kemper<sup>c</sup>, and Zhiyou Jing<sup>d\*</sup>

<sup>a</sup>*Key Laboratory of Marine Hazards Forecasting, Ministry of Natural Resources, Hohai University, Nanjing, China*

<sup>b</sup>*College of Oceanography, Hohai University, Nanjing, China*

<sup>c</sup>*Department of Earth, Environmental, and Planetary Sciences, Brown University, Providence, RI, USA*

<sup>d</sup>*State Key Laboratory of Tropical Oceanography, South China Sea Institute of Oceanology, Chinese Academy of Sciences, Guangzhou, China*

Corresponding author: Zhiyou Jing (jingzhiyou@scsio.ac.cn)

## ABSTRACT

The submesoscale energy budget is complex and remains understood only in region-by-region analyses. Based on a series of nested numerical simulations (ROMS0, ROMS1, and ROMS2), this study investigated the submesoscale energy budget and flux in the upper ocean of the Kuroshio Extension, including some innovations for examining submesoscale energy budgets in general. The ROMS2 simulation on a  $\sim 500$  m grid resolves a variety of submesoscale instabilities allowing an energetic analysis in the submesoscale range. The frequency–wavenumber spectra of vertical vorticity variance (i.e., enstrophy) and horizontal divergence variance were used to identify the scales of submesoscale flows as distinct from those of inertia-gravity waves but dominating horizontal divergence variance. Next, the energy transfers between the background scales and the submesoscale were examined. The submesoscale kinetic and potential energy (SMKE and SMPE) were mainly contained in the mixed layer and energized through both barotropic (shear production) and baroclinic (buoyancy production) routes. Averaged over the upper 50 m of ROMS2, the baroclinic transfers amounted to approximately 75% of the sources for the SMKE ( $3.42 \times 10^{-9}$  W/kg) versus the remaining 25% ( $1.12 \times 10^{-9}$  W/kg) via barotropic downscale KE transfers. The KE field was greatly strengthened by energy sources through the boundary—this flux is larger than the mesoscale-to-submesoscale transfers in this region. Spectral energy production, importantly, reveals upscale KE transfers at larger submesoscales and downscale KE transfers at smaller submesoscales (i.e., a transition from inverse to forward KE cascade). This study seeks to extend our understanding of the energy cycle to the submesoscale and highlight the forward KE cascade induced by upper-ocean submesoscale activities in the research domain.

## 36 1. Introduction

37 Submesoscale activities are ubiquitous in high-resolution satellite images and have  
38 received intense study via simulations and observations in recent decades. Oceanic energy  
39 cascade research beforehand tended to emphasize the large scale of climatological forcing,  
40 the mesoscale with its dominant reservoir of kinetic energy and paradoxical inverse cascade  
41 (Ferrari and Wunsch 2009), and the forward cascade of internal waves and microstructure  
42 turbulence. Recent studies have highlighted the role of submesoscale processes and their  
43 instabilities, as a dynamic conduit for energy transfer between large-scale and dissipation  
44 scale (e.g., Capet et al. 2008a; Thomas et al. 2013; McWilliams 2016; Wang et al. 2018) and  
45 as a mechanism for vertical transport of heat, salt, and biogeochemical tracers (e.g.,  
46 Mahadevan and Tandon 2006; Lévy et al. 2001, 2012; Rosso et al. 2014). However,  
47 challenges associated with studying submesoscales remain (McWilliams 2016), as in-situ  
48 observations of quickly evolving, intermittent events over  $O(1\text{--}10\text{ km})$  scales are rarely clear  
49 from cruise surveys or moorings, although drifters, autonomous platforms, and new remote  
50 sensing are improving submesoscale observation techniques (e.g., D’Asaro et al. 2020;  
51 Gentemann et al. 2020; Villas Boas et al. 2019; du Plessis et al. 2019). In realistic numerical  
52 simulations, the horizontal grid resolution has been too coarse to capture submesoscale flows  
53 adequately until recently (Dong et al. 2020a).

54 Identifying the dynamical routes for removal of large-scale energy is a challenge.  
55 Quasigeostrophic and 2D turbulence roughly following a  $k^{-5/3}$  power law are characterized by  
56 an inverse energy cascade at large scales and a forward potential enstrophy cascade with  
57 minimal forward kinetic energy transfer ( $k^{-3}$  power law) in the homogenous, isotropic  
58 turbulence limit (e.g., Kraichnan 1967; Charney 1971; Cronin and Watts 1996; Tulloch et al.  
59 2011; Kang and Curchitser 2015; Yang and Liang 2016; Pearson and Fox-Kemper 2018). In  
60 mesoscale-permitting models, the primary sinks of kinetic energy are bottom drag and  
61 vertical mixing, although cascade processes as represented through parameterizations may  
62 play a role (Pearson et al. 2017).

63 Thus, submesoscale processes are expected to be a mechanism for the downscale energy  
64 transfer (Ferrari and Wunsch 2009), either by barotropic kinetic energy transfers or by  
65 baroclinic mechanisms linking to potential energy transfers (Capet et al. 2008; Fox-Kemper  
66 et al. 2008). For example, surface-trapped modes (Klein et al. 2008) can easily drive  
67 submesoscale flows with Rossby and Richardson numbers of  $O(1)$  (Thomas et al. 2008) by a

68 variety of submesoscale instabilities such as mixed layer instability (Boccaletti et al. 2007;  
69 Fox-Kemper et al. 2008), symmetric instability that draws energy from geostrophic shear  
70 production (Hoskins 1974; Thomas et al. 2013; Bachman et al. 2017a), lateral shear  
71 instability and barotropic conversion (Munk et al. 2000; Fox-Kemper et al. 2008; Molemaker  
72 et al. 2010; Gula et al. 2014), and centrifugal instability (Jiao and Dewar 2015). In some  
73 regions and simulations, submesoscales may even energize the mesoscale (Callies et al. 2016;  
74 Schubert et al. 2020). These instabilities form from and influence the flow shear, frontal  
75 strength, and mixed layer depth. The OSMOSIS mooring observations in the eastern North  
76 Atlantic indicate that submesoscale eddies are mainly generated through baroclinic instability  
77 with energy from buoyancy production (Buckingham et al. 2017), whereas Wang et al. (2018)  
78 showed that submesoscale eddies in the tropical Pacific Ocean on a scale of 300 km are  
79 generated through barotropic instability of the geostrophic shear. In situ observations (e.g.,  
80 Callies et al. 2015; Buckingham et al. 2016; Thompson et al. 2016; Jing et al. 2016; D’Asaro  
81 et al. 2020) and high-resolution numerical simulations (e.g., Capet et al. 2008b; Klein et al.  
82 2008; Sasaki et al. 2014; Gula et al. 2016; Bachman et al. 2017b; Schubert et al. 2020) all  
83 suggest that submesoscales in the ocean form a continuum of chaotic nonlinear processes  
84 (Shcherbina et al. 2013), exhibiting regional uniqueness that is difficult to disentangle.

85 To manage the variety of submesoscale instabilities, an energy flow analysis was used to  
86 separate the barotropic and baroclinic energy routes in regions such as the Kuroshio  
87 Extension. The energetic Kuroshio Extension jet flows eastward from the coast of Japan  
88 maintaining a meandering pattern with the highest energy level of mesoscale eddies in the  
89 Northwest Pacific Ocean (Tai and White 1990; Qiu et al. 1991; Qiu 2000; Nakamura and  
90 Kazmin 2003; Qiu 2005) and exchanges momentum and water masses in the Kuroshio  
91 Extension region (Qiu and Chen 2005; Waterman and Jayne 2011). The jet and its mesoscale  
92 features are favorable for generating submesoscales through both baroclinic and barotropic  
93 routes (Sasaki et al. 2014; Qiu et al. 2014). A series of nested numerical simulations used  
94 here (ranging from ROMS0 at ~7.5 km resolution to ROMS2 at ~0.5 km) permit most  
95 geostrophic-branch barotropic and baroclinic submesoscale instabilities in the Kuroshio  
96 Extension region during the late spring (fully described in Section 2a; Jing et al. 2020; Dong  
97 et al. 2020a). These high-resolution simulations were used to study the spectral energy budget  
98 and transfer routes near the strong persistent front.

99 This modeling study has four main goals: (1) Defining the submesoscale range in  
100 frequency–wavenumber space, as inspired by examining the spectra of vorticity and

101 divergence which reveals the submesoscale as a region of elevated divergence. (2) Clarifying  
102 the barotropic and baroclinic energy transfer routes by presenting the energy cycle  
103 emphasizing flows into the submesoscale range. (3) Identifying the dominant energy routes  
104 energizing submesoscales in the Kuroshio Extension region. (4) Quantifying the scale-  
105 dependent kinetic and potential energy fluxes with spectral energy budgets.

106 The remainder of this paper is organized as follows. Section 2 describes the model setup,  
107 validates the model skill with satellite and in-situ observations, and frames the analysis  
108 method. Section 3 identifies, separates, and quantifies the submesoscale kinetic energy  
109 (SMKE) and potential energy (SMPE), exploiting the frequency–wavenumber spectra of  
110 kinetic energy, potential energy, vertical vorticity variance (i.e., enstrophy), and horizontal  
111 divergence variance. Section 4 presents a detailed energy budget analysis of the upper ocean  
112 submesoscales and also investigates the wavenumber spectra of the components making up  
113 the barotropic and baroclinic energy fluxes and their sensitivity to horizontal resolution.  
114 Finally, Section 5 summarizes the conclusions of this study.

115

## 116 **2. Model description and analysis method**

### 117 *a. High-resolution simulation and validation*

118 In this study, the Regional Oceanic Modeling System (ROMS) is used to conduct a series  
119 of one-way-nested simulations of the Kuroshio Extension (Shchepetkin and McWilliams  
120 2005). The parent model (ROMS0) with a coarse horizontal resolution of  $\sim 7.5$  km covers the  
121 northwest Pacific Ocean (Fig. 1a) and a 20-year spin-up was performed to reach a statistically  
122 steady state before starting the one-way nesting simulations on child grids of  $\sim 1.5$  km  
123 (ROMS1) and  $\sim 0.5$  km (ROMS2). For brevity, the simulations are also referred to as low-,  
124 middle-, and high-resolution simulations. These simulations were run on a curvilinear,  
125 latitude–longitude grid and terrain-following S-coordinates of 60 vertical levels. In these  
126 simulations, surface atmospheric forcing including wind stress, heat, and freshwater fluxes,  
127 were derived from the daily mean climatology of the Quick Scatterometer (QuikSCAT)  
128 dataset and the International Comprehensive Ocean Atmosphere Data Set (ICOADS)  
129 (Woodruff et al. 2011). The boundary and initial information for the largest domain were  
130 taken from the monthly averaged Simple Ocean Data Assimilation (SODA) ocean  
131 climatology outputs (Carton and Giese 2008). The K-profile parameterization (KPP) was

used to represent the sub-grid vertical mixing of momentum and tracers (Large et al. 1994). The modeling results (e.g., regional circulation, mixed layer depth, and energy level of mesoscale eddies) have been validated against satellite measurements and limited in situ observations. Comparisons to measurements on multiple platforms show that the simulations are sufficiently accurate to characterize the climatological conditions of the northwest Pacific upper ocean. ROMS1 (~1.5 km) was run for one year and provided daily boundary information for the nested simulation of ROMS2 that lasts two weeks from April 28 to May 12 (capturing a quasi-stationary period for the meandering flow of the Kuroshio Extension). Therefore, the energy level of submesoscales remained steady without seasonal variation during this period. As shown in the following sections, the 2-hourly output from ROMS2 can clearly depict the evolution of larger submesoscale motions, although smaller submesoscale instabilities are likely affected by resolution (Bachman and Taylor 2014).

The research domain is shown in Fig. 1a. Figs. 1b and c compares the ROMS2 surface temperature to the MODIS-Aqua data from <https://oceancolor.gsfc.nasa.gov/> in the same month (May 1, 2018). The simulated temperature field roughly agrees with the satellite observation. In addition, the location of the flow stream and the scale of the meander in the simulation are close to those in the satellite image. The in-situ velocity data observed by the mooring of the Kuroshio Extension System Study (KESS) project (available at <https://uskess.whoi.edu/overview/dataproducts/>) were used to validate the kinetic energy (KE) level of the simulation (Fig. 1d). The KE spectra of the mooring observation and the simulation are comparable in amplitude and spectral slope, although the tidal frequencies were underestimated because of the absence of tidal forcing in the simulation.

#### 154 *b. Energetic diagram*

Energetics analysis quantifies the energy budget: the energy sources, sinks, and exchanges among different energy reservoirs. To examine the energy exchange between submesoscale and larger and/or slower scales (called the “background” to denote that it can contain small and slow or large and fast scales), the following energy equations were derived from the hydrostatic, Boussinesq equations for seawater:

$$160 \quad \frac{\partial u}{\partial t} + \mathbf{u} \cdot \nabla u - f v = -\frac{1}{\rho_0} \frac{\partial p}{\partial x} + F_u + D_u, \quad (1)$$

$$\frac{\partial v}{\partial t} + \mathbf{u} \cdot \nabla v + fu = -\frac{1}{\rho_0} \frac{\partial p}{\partial y} + F_v + D_v, \quad (2)$$

$$\frac{\partial p}{\partial z} = -\rho g, \quad (3)$$

$$\frac{\partial C}{\partial t} + \mathbf{u} \cdot \nabla C = F_c + D_c, \quad (4)$$

$$\nabla \cdot \mathbf{u} = 0, \quad (5)$$

where  $\mathbf{u}=(u,v,w)$  is the velocity vector,  $f$  is the Coriolis frequency,  $\rho$  is the density,  $\rho_0=1025 \text{ kg m}^{-3}$  is the reference density, and  $p$  denotes the pressure. The last two terms in Eqs. (1), (2), and (4),  $F$  and  $D$ , represent the forcing and dissipation respectively, which include viscosity, diffusivity, and subgrid parameterizations. The tracer equation, Eq. (4), holds for salinity and temperature, where the density is calculated using the nonlinear equations of state. A Reynolds decomposition for 3D flow is employed to separate the background flow and submesoscale perturbations as

$$\mathbf{u} = \bar{\mathbf{u}} + \mathbf{u}' \quad (6)$$

The eddy state has been commonly derived from the time-mean or spatial filtering of the velocity field in previous studies of energetics (Cronin and Watts 1996; Aiki and Richards 2008; Grooms et al. 2013). In this study, the perturbation velocity was derived by both high-pass filtering in time and spatial domains, with a sharp spectral cutoff in the Fourier transform spectrum to make an approximate Reynolds average. The specific scale and frequency partition is marked in the frequency–wavenumber spectrum in Fig. 4. Then, the residual flow was considered as the background flow (indicated by the overbar in Eq. (6)), which contains large, slow variability, but also large, fast variability and small, slow variability.

The length scale of submesoscale instabilities in the mixed layer can be estimated by (Boccaletti et al. 2007)

$$L = \frac{NH_m}{f} \sqrt{1 + 1/Ri}, \quad (7)$$

where  $H_m$  is the depth of the mixed layer and  $N$  is the buoyancy frequency. Also, the linear instability time scale can be estimated by (Callies et al. 2015)

$$T = \frac{N}{f \sqrt{(\partial \bar{u} / \partial z)^2 + (\partial \bar{v} / \partial z)^2}}, \quad (8)$$

In submesoscale turbulence, cascades alter the energy-containing length scale and the eddy turnover time significantly away from these linear instability values (Fox-Kemper et al. 2008, Bachman and Fox-Kemper 2013). Thus, a different method for identifying the nonlinear cascade range of scales constituting the submesoscales is needed.

As previously mentioned, the smaller submesoscales and 3D turbulence are parameterized, so the submesoscales are expected to represent the smallest resolved scales in ROMS2. With these guidelines in mind, high-pass filtering in both time and space was conducted to obtain the high-wavenumber, high-frequency perturbation (primed in Eq. (6)) velocities that are defined as submesoscale flows, not based on linear instability scales but on energy-containing scales. The common emphasis for submesoscales is their intense vorticity (Capet et al. 2008b; Thomas et al. 2008) and divergence (D'Asaro et al. 2016, 2018; Pearson et al. 2019, 2020), which will serve as the basis for targeting their range of scales. In our analysis, the submesoscale is defined as a horizontal scale of less than 20 km and also a time scale of less than 1.5 days. A detailed analysis of choosing these particular bounds for the definition of the submesoscale follows in Section 3.

After the Reynolds averages are defined, the KE budget by submesoscale perturbations can be obtained by multiplying momentum Eqs. (1) and (2) by  $\rho_0 u'$  and  $\rho_0 v'$ , respectively, and taking the Reynolds average of their sum gives

$$\begin{aligned} \frac{\partial}{\partial t} (\text{SMKE}) = & \underbrace{-\frac{1}{2} \rho_0 \nabla \cdot [\mathbf{u}(u'^2 + v'^2)]}_{\text{ADK}} \underbrace{- \nabla \cdot (\mathbf{u}' p')}_{\text{PW}} \\ & \underbrace{- \overline{g \rho' w'}}_{\text{PKE}} \underbrace{- \rho_0 (\mathbf{u}' \mathbf{u}' \cdot \nabla \bar{\mathbf{u}} + \mathbf{v}' \mathbf{u}' \cdot \nabla \bar{\mathbf{v}})}_{\text{BSK}} + \underbrace{\overline{D_{K2}} + \overline{F_{K2}}}_{\text{D+F}}, \end{aligned} \quad (9)$$

where SMKE refers to the hydrostatic submesoscale kinetic energy,  $(\rho_0 u'^2 + \rho_0 v'^2)/2$ . The cross energy terms are negligible (e.g.,  $\overline{\mathbf{u}' \cdot \bar{\mathbf{u}}} \approx 0$ ), because the average is assumed to be a Reynolds average. The first and second terms on the right side represent the advection of and pressure work on SMKE (ADK and PW), respectively. The third term represents the buoyancy production, which is the energy conversion from SMPE to SMKE, which is typical of baroclinic instability pathways (hereafter referred to as PKE). The fourth term denotes the shear production, i.e., energy transfer from large-scale KE to SMKE through submesoscale



214 rearrangement of momentum that changes the large-scale shear, also known as the barotropic  
 215 instability pathway (background-to-submesoscale KE transfer, hereafter referred to as BSK).  
 216 Note that both horizontal and vertical shear production are counted in BSK.  $D_{K2}$  and  $F_{K2}$  are  
 217 the diffusion and forcing of SMKE, which are calculated as the residual of the other terms in  
 218 the energy budget equation.

219 Similarly, the potential energy (PE) budget by the submesoscale perturbations can be  
 220 expressed as

$$221 \quad \frac{\partial}{\partial t}(\text{SMPE}) = \underbrace{-\nabla \cdot \left[ \mathbf{u} \left( \frac{g^2 \rho'^2}{2\rho_0 N^2} \right) \right]}_{\text{ADP}} - \underbrace{\frac{g^2}{\rho_0 N^2} \overline{\rho' \mathbf{u}' \cdot \nabla \rho}}_{\text{BSP}} + \underbrace{\overline{g \rho' w'}}_{-\text{PKE}} + \underbrace{\overline{D_{P2}} + \overline{F_{P2}}}_{\text{D+F}}, \quad (10)$$

222 where a linear definition for the available potential energy (APE) is used (Gill 1982; Kang  
 223 and Fringer 2010) as follows,

$$224 \quad APE = \frac{g^2 (\rho - \rho_r)^2}{2\rho_0 N^2}, \quad (11)$$

225 where  $\rho_r$  is the reference density. Based on these definitions, the SMPE can be expressed as

$$226 \quad \text{SMPE} = \frac{g^2 \rho'^2}{2\rho_0 N^2}. \quad (12)$$

227 The SMPE budget equation results from using a locally linear state equation to arrive at a  
 228 tracer equation for density in the same form as Eq. (4), i.e., neglecting nonlinear thermosteric  
 229 effects such as cabbelling. Note that a completely satisfactory definition of APE  
 230 corresponding to the Lorenz (1955) approach does not exist for seawater (Huang 1999), but  
 231 this approach is negligibly different from other more computationally expensive ones (Saenz  
 232 et al. 2015), especially at the ocean surface where the submesoscales are highly active,  
 233 compressibility effects are small, and this energy budget is evaluated. These definitions were  
 234 selected for ease of comparison with approaches taken in other basins (Kang and Fringer  
 235 2010; Kang and Curchitser 2015). In this study, these budgets were calculated only over the  
 236 upper 50 m surface region of ROMS2 over the whole zonal and meridional region. The terms  
 237 on the right-hand side of Eq. (10) represent the advection (ADP), buoyancy production  
 238 energy conversion from SMPE to SMKE (again typical of baroclinic instability pathways, -  
 239 PKE), submesoscale horizontal buoyancy production (BSP), and diffusion and forcing that  
 240 are determined by the residual. The two energy equations provide an estimate of the

241 submesoscale energy production terms. An energy budget diagram (Fig. 2) is employed to  
 242 chart the energy conversion between the submesoscale and background scales.

243 The large and slow scales, including the mesoscales, are the primary reservoir and  
 244 constitute the background potential and kinetic energy, referred to as BPE and BKE  
 245 respectively. In Fig.2, BSK and BSP represent the KE and PE transfer from background  
 246 scales to the submesoscale (Kang and Curchitser 2015; Yan et al. 2019). BSK and BSP have  
 247 also been widely interpreted as barotropic (shear production) and baroclinic (buoyancy  
 248 production) energy conversions to smaller scales (e.g., Cronin and Watts 1996; Kang and  
 249 Curchitser 2015). The green arrows denote the combined effects of atmospheric forcing and  
 250 dissipation, which are estimated by the residual of the other terms.

251 The energy budget of the background scales is formed by finding the Reynolds average  
 252 momentum equation and forming a mean energy equation from its dot product with  $\rho_0 \bar{\mathbf{u}}$ .  
 253 Collecting the key terms from the energy budget formed from the Reynolds averaged Eqs. (1-  
 254 5), we obtain

$$255 \quad \text{SBK} = -\overline{\rho_0 (\bar{\mathbf{u}} \nabla \cdot (\mathbf{u}' \mathbf{u}') + \bar{\mathbf{v}} \nabla \cdot (\mathbf{u}' \mathbf{v}'))} = \text{BndyKE} - \text{BSK}, \quad (13)$$

$$256 \quad \text{SBP} = -\frac{g^2}{\rho_0 N^2} \overline{\rho \nabla \cdot \mathbf{u}' \rho'} = \text{BndyPE} - \text{BSP}. \quad (14)$$

257 SBK and SBP are also known as the background kinetic and potential energy change due to  
 258 eddy momentum fluxes (i.e., Reynolds stresses) and density fluxes (Chen et al. 2014).

259 Calculus identities guarantee that the term formed by the dot product with the Reynolds  
 260 stress is equal and opposite to the shear production in a closed basin, when the global  
 261 integrals of the boundary terms (BndyKE, BndyPE) are guaranteed to be zero (Chen et al.  
 262 2014). However, for a fractional basin ocean domain, these boundary terms can and do  
 263 provide additional sources and sinks for the energy budget. In an open domain, the sum of  
 264 SBK and BSK (or SBP and BSP) tends to be non-zero but instead equals a boundary term  
 265 contributing to the KE (PE) field. Care is needed, and there is a choice to which reservoir  
 266 BndyKE and BndyPE are applied. Here we chose to interpret BndyKE as a source to the  
 267 BKE, which results in the BSK transfer energizing the SMKE (and SBK playing a less  
 268 important role). Similarly, we chose to interpret BndyPE as energizing the BPE, which then  
 269 makes BSP the path to energizing the SMPE. See APPENDIX for a more detailed derivation  
 270 and discussion.

271

### 272 **3. Submesoscale kinetic and potential energy**

#### 273 *a. Energy levels of BKE, SMKE, and SMPE*

274 This section estimates the energy levels of BKE, SMKE, and SMPE. BPE cannot be  
275 estimated without an arbitrary definition of reference level. Fig. 3 shows the energy levels of  
276 BKE, SMKE, and SMPE averaged over the upper 50 m of the research domain from the  
277 ROMS2 simulation. It shows that the submesoscale energy (SMKE + SMPE) is orders of  
278 magnitude smaller than the BKE and that SMKE + SMPE tends to be stronger where the  
279 BKE is large, as the energetic background flow is favorable for generating submesoscales. As  
280 shown in Fig. 3d, the KE spectrum has a slope of  $-2.4$  from mesoscale to submesoscale in the  
281 mixed layer and the slope drops to  $-3$  (geostrophic prediction) below the mixed layer. The  
282 flattening of the mixed layer KE spectrum is thought to arise from the submesoscale motions,  
283 especially fronts (Capet et al. 2008b). However, the spectral roll-off starting from  $\sim 5$  km is  
284 not consistent with observations, thus, the spectra below 5 km (about ten times the grid size)  
285 presumably result from a numerical issue leading to the excessive damping of KE at scales  
286 smaller than 5 km. Fortunately, the submesoscales in this region reach up to 20 km for about  
287 a half-decade of reliable submesoscale dynamics. In the depth-averaged horizontal plane (Fig.  
288 3e), the jet region (between  $33$  and  $37^\circ\text{N}$ ) has more energetic BKE, SMKE, and SMPE,  
289 among which the BKE is approximately two orders of magnitude larger than the SMKE or  
290 SMPE. As seen from the horizontally averaged vertical profile (Fig. 3f), the SMKE and  
291 SMPE underwent a dramatic decrease from  $1.17 \times 10^{-3}$  J/kg and  $0.90 \times 10^{-3}$  J/kg at the  
292 surface to  $0.50 \times 10^{-3}$  J/kg and  $0.31 \times 10^{-3}$  J/kg at the base of the mixed layer, respectively,  
293 indicating that the submesoscale energy is higher in the mixed layer. The average mixed layer  
294 depth marked by the red dashed line is defined to be the shallowest depth where the density  
295 difference is  $0.03 \text{ kg m}^{-3}$  from the surface layer (de Boyer Montégut et al. 2004), and the  
296 energy budget will be taken over the upper 50 m, including the entire mixed layer and some  
297 of the pycnocline.

#### 298 *b. Spectral estimates of the submesoscale range*

299 A further look into the kinetic and potential energy can be achieved by the spectra as  
300 functions of frequency and wavenumber defined by

$$KE = \frac{1}{2} \hat{\mathbf{u}}^* \cdot \hat{\mathbf{u}} \quad PE = \frac{1}{2} \hat{b}^* \hat{b} / N^2, \quad (15)$$

where  $b = -g(\rho / \rho_0)$  is the buoyancy and  $\hat{\cdot}$  denotes the Fourier transform. The frequency–wavenumber (F–K) spectrum can be derived from the model data using these definitions. The details of deriving the spectrum can be found in Cao et al. (2019). In Fig. 4, both the kinetic and potential energy continuously decrease (ROMS2 simulation at  $z = -5$  m) from larger, slower to smaller, quicker scales along the wavenumber or frequency axis. The submesoscale range used in this study is also marked by the grey-line rectangle boxes, and the blue double arrows denote the energy exchange between different spaces. In Fig. 4, no clear submesoscale energy peak is recognizable in either of the spectra, as SMKE or SMPE is orders of magnitude smaller than the mesoscale energy. This is consistent with the 1-D wavenumber spectrum and energy content figures (Fig. 3). Instead, the vertical vorticity ( $\zeta = \frac{\partial v}{\partial x} - \frac{\partial u}{\partial y}$ ) variance (or enstrophy) and horizontal divergence ( $\text{Div.} = \frac{\partial u}{\partial x} + \frac{\partial v}{\partial y}$ ) variance spectra (formed from the Fourier transforms of vorticity and divergence just as the energy spectra are formed from velocity and buoyancy) more clearly isolate the submesoscales as those with high density of vorticity and divergence variability.

The submesoscales have pronounced rotational and divergent effects at submesoscales (e.g., Pearson et al. 2017; Torres et al. 2018; Cao et al. 2019), which are reflected in the enstrophy and divergence variance F–K spectra. As shown in Fig. 5a, the normalized enstrophy F–K spectrum at the near-surface layer ( $z = -5$  m) displays two remarkable peaks, reflecting the F–K regions of the mesoscale and submesoscale eddies, respectively, due to their high vorticity concentrations. Furthermore, the submesoscale enstrophy spectrum peak coincides with the divergence variance spectrum peak (Figs. 5a,b), suggesting the quasigeostrophically-unbalanced convergence of submesoscale motions. Dynamically, submesoscales differ from mesoscales as characterized by an enhancement of horizontal divergence associated with their higher Rossby number allowing them to have stronger ageostrophic transport (D’Asaro et al. 2018).

Notably, the enstrophy and divergence variance spectra rationalize our selected scale partition to isolate the submesoscales. The horizontal divergence reaches its maximum at wavelengths of  $\sim 8$  km, which is wrapped in the defined submesoscale range ( $< 20$  km) in this

study. Compared to the near-surface spectra within the mixed layer, the submesoscale vorticity at 200-m depth is dramatically reduced, while the mesoscale vorticity remains high, indicative of energetic mesoscale eddy effects near 100 km (a comparison between Figs. 5a,c). A typical requirement for the development of submesoscale instabilities is the low stratification in the mixed layer (Boccaletti et al. 2007; Fox-Kemper et al. 2008; Thomas et al. 2008), where the energetic submesoscale divergence arises from the submesoscale fronts and instabilities and through turbulent cascades develops broadband power-law-like spectra. While in the deeper layers, inertia-gravity waves become important for the horizontal divergence (Torres et al. 2018) and appear as energized wave-banded regions of the F-K spectrum where the free, linear inertia-gravity wave dispersion relations lie. The divergence variance spectrum below the mixed layer (Fig. 5d) shows a weak but distinct banded divergence signal in the high-frequency, low-wavenumber space (highlighted by an ellipse): the signature of inertia-gravity waves. Within the mixed layer (Fig. 5b), the gravity wave signal is not apparent. Note that inertia-gravity wave motions are expected to be underestimated because of the absence of high-frequency wind stresses and tidal forcing in the simulation.

346

## 347 **4. Energy budget analysis and discussion**

### 348 *a. Submesoscale kinetic energy budget*

349 The high-resolution model output allows an estimate of each form of SMKE production (background-to-submesoscale KE transfer: BSK, advection of KE: ADK, buoyancy production: PKE, and pressure work: PW, respectively). In Fig. 6, these energy production terms delineate the submesoscale eddy variability with positive/negative values denoting the submesoscale energy generation/sink. They are more active along the jet than at the flanks. This is because the jet enhances the flow shear and forms a large-scale front with great horizontal buoyancy gradient, which is favorable for the generation of submesoscales via baroclinic instability and frontogenesis.

357 In Fig. 6a, the BSK—a combination of the effects of Reynolds stress, horizontal and vertical shear, and the BndyKE influence of outer domains—is intensified near the jet with a positive-negative pattern that can be interpreted as the injection (positive values) and loss (negative values) of SMKE. The eddy-mean interaction is complicated because various

361 processes underlie bidirectional energy transfers (i.e., forward energy transfer is driven by  
 362 submesoscale instabilities; while the flow strain could stabilize the horizontal shear instability  
 363 and cause an energy transfer from submesoscale kinetic energy to the background kinetic  
 364 energy (negative BSK: Gula et al. 2014; Brannigan et al. 2017), or high-frequency eddies can  
 365 interact to drive lower frequency motions (Arbic et al. 2014). In contrast, the submesoscale  
 366 PKE—known to generate SMKE from baroclinic instability modes—is mostly positive in the  
 367 research domain, indicative of a continuous energy transfer from SMPE to SMKE associated  
 368 with processes such as mixed layer instability (Fox-Kemper et al. 2008) and frontogenesis  
 369 (e.g., Capet et al. 2008a; Suzuki et al. 2016). PW is positive in the upper layers, acting to  
 370 energize the submesoscale flows; conversely, the negative PW in the lower layers partially  
 371 balances the PKE, acting to stabilize the base of the mixed layer. The SMKE is reduced by  
 372 PW during mixed layer restratification, which tends to restore geostrophy (Cao and Jing  
 373 2020). In the zonally averaged plots (Fig. 7), the BSK is highly intensified in the surface  
 374 boundary layers at the jet, but the PKE can energize the whole mixed layer and reaches its  
 375 maximum in the middle of the mixed layer as in parameterization theory (Fox-Kemper et al.  
 376 2008). The mean mixed layer depth is marked by dashed lines in the figures. PKE and BSK  
 377 are the largest and second largest producers of SMKE, respectively. The net contribution of  
 378 PW and ADK is minor (submesoscale advection is not important in our research domain),  
 379 which is fortunate due to uncertainties in the interpretation of energy sources these terms can  
 380 induce (Plumb 1983). The BndyKE source is large, but in the chosen framing where it is  
 381 applied to the BKE, only BSK needs to be analyzed in the SMKE budget.

382 In the zonal-mean, latitude-vertical section plot (Fig. 8a), the ADK presents a modest  
 383 positive impact in the south but a negative impact in the north, indicating opposing effects on  
 384 the two flanks of the jet. It is unclear why this pattern exists—it may be a coincidence of the  
 385 location of the eddies incompletely cancelling (Fig. 6). In the vertical profile (Fig. 8b),  
 386 submesoscale energy production occurs mainly in the mixed layer for most terms. Among  
 387 them, the PW yields a significant energy input in the surface boundary layer of 0–15 m but  
 388 remarkable negative work at depths of 20–50 m, indicating vertical transfer of submesoscale  
 389 energy. The negative work tends to reduce the submesoscale kinetic energy at the base of the  
 390 mixed layer and opposes the PKE there (Fig. 8b), although the vertically integrated  
 391 contribution of pressure in the mixed layer is not of great importance.

## 392 *b. Submesoscale potential energy budget*

393 Figs. 9, 10, and 11 show the horizontal and vertical distributions of BSP and ADP  
 394 production, respectively, as in the SMPE equation. Removal of SMPE by PKE is not shown  
 395 because it is already shown as a production of SMKE in the previous section and Figs. 6, 7,  
 396 and 8. The BSP averaged over the upper 50 m (Fig. 9a) was mostly positive in the research  
 397 domain and intensified near the flow stream, consistent with the distribution of PKE. Thus,  
 398 BSP—energy conversion from BPE to SMPE—serves as an important energy source for  
 399 SMPE in the energy cycle (Fig. 2), probably arising from the horizontal concentration of  
 400 density gradients by frontogenesis, submesoscale eddies, and winds. The BSP is also  
 401 enhanced at the jet, which essentially results from the arrestment of cold filaments by  
 402 horizontal shear instability (Gula et al. 2014). In a zonal-mean, vertical section plot (Fig. 10),  
 403 the BSP mainly occurs in the middle of the mixed layer, consistent with the distribution of  
 404 PKE. In contrast, the averaged ADP is small and seems to be insignificant for net SMPE  
 405 production either in the latitude-dependent plot or in the horizontally averaged vertical profile  
 406 (Fig. 11). Besides, ADP shows an opposite dependence on latitude than ADK (the orange line  
 407 in Fig. 11a versus the yellow line in Fig. 8a); thus, the overall advection, a sum of ADP and  
 408 ADK, has a slight contribution to the submesoscale energy. BndyPE is a nontrivial source of  
 409 potential energy; however, unlike BndyKE, it is not sufficiently strong to affect the direction  
 410 of energy flow from the BPE to the SMPE, i.e., both BSP and SBP agree that the potential  
 411 energy transfer is toward smaller, faster scales.

### 412 *c. Energy pathways to the submesoscale*

413 Fig. 12 summarizes the upper-ocean energy cycle between the larger and slower  
 414 background scales and the submesoscale. In the ROMS2 simulation (Fig. 12b), the  
 415 submesoscale contains  $0.69 \times 10^{-3}$  J/kg of SMKE, followed by SMPE with an amount of  $0.51$   
 416  $\times 10^{-3}$  J/kg. The energy cycle displays two dominant, distinct routes of SMKE generation:  
 417 BKE→SMKE through BSK and BPE→SMPE→SMKE through BSP and PKE. Statistically,  
 418 the baroclinic energy conversion from SMPE to SMKE through PKE (3.42 in units of  $10^{-9}$   
 419 W/kg) accounts for ~75% of the SMKE generation, dominating the possible direct wind-  
 420 forced SMKE. Note that the direct wind stress effects on the submesoscale energy, SMKE  
 421 and SMPE, are estimated to be minor compared to other effects. Since none of the PW ( $0.61$   
 422  $\times 10^{-9}$  W/kg) and ADK ( $0.02 \times 10^{-9}$  W/kg) are large enough to balance the SMKE, the  
 423 remaining energy goes to parameterized dissipation ( $3.91 \times 10^{-9}$  W/kg), estimated by  
 424 assuming the SMKE is constant during the period ( $\partial \text{SMKE} / \partial t = 0$ ). The BSP provides about

425 60% of the SMPE that is subsequently transferred to SMKE through PKE, implying that a  
426 substantial portion of SMPE comes from the large-scale potential energy field (Fig. 12a).  
427 These results provide an important clue to the underlying submesoscale processes and their  
428 effects on the energy cycle (discussed in the following section). Note that the PKE is larger  
429 than the BSP (Fig. 12a), suggesting external submesoscale energy injection to SMPE, for  
430 example through wind forcing stimulating frontogenesis (Thomas et al. 2008).

431 A rough estimate suggests that it takes approximately 1.76 days by the BSK and PKE  
432 together to fuel the SMKE reservoir as observed regardless of the other effects. This  
433 production timescale approximates the length of the life cycle of submesoscale features. The  
434 submesoscales are fast-evolving and hardly retained if sources of energy were removed (see  
435 Suzuki et al. 2016 for a decay time estimate for submesoscale fronts). The submesoscale  
436 forward energy conversion rate in the mixed layer can reach a magnitude of  $10^{-9}$  W/kg,  
437 comparable to the order of mesoscale effects estimated by Yang and Liang (2016) and  
438 submesoscale-induced turbulent dissipation rates found by D'Asaro et al. (2011) near the  
439 Kuroshio Extension. In contrast, mesoscale turbulence is normally characterized by an  
440 inverse KE cascade, whereas here a significant forward transfer from the background to the  
441 submesoscales is found.

442 Note that there exists a remarkable energy source for the KE ( $4.90 \times 10^{-9}$  W/kg) and a  
443 slight energy leakage for the PE ( $0.21 \times 10^{-9}$  W/kg) through the boundary in ROMS2. It is  
444 easiest to consider the significant BndyKE as a strong flux of energy from adjacent ocean  
445 domains that energizes the BKE field, which in turn energizes the submesoscale via BSK.  
446 However, if the convention for BndyKE is taken as arriving first in the SMKE, this  
447 interpretation implies a large positive SBK ( $3.78 \times 10^{-9}$  W/kg), indicating an inverse energy  
448 flow from the submesoscale to the background, while submesoscales are being strengthened  
449 by the KE field outside of the model domain. It is frankly confusing that the boundary source  
450 of KE is so large as to reverse the interpreted direction of transfer between the submesoscale  
451 and background scale based on a choice of convention. If the simulated region was bounded,  
452 there would be no interpretation required as the boundary terms would vanish. It is unclear to  
453 what extent an open domain plays a role in the interpretation of inverse and direct cascades in  
454 other studies (e.g., Schubert et al. 2020). The boundary source of PE is small enough to cause  
455 less confusion, as at least SBP and BSP share the same direction from BPE to SMPE.

456 A comparison between the different resolution simulations ROMS2 and ROMS1 shows  
457 that most submesoscale energy production terms decrease in the lower-resolution simulation



except for a slight increase in BSK. As mentioned above, BSK is an ensemble of several cancellatory effects, so one possible reason for an increase at coarser resolution is that the sub-components of BSK fail to fully cancel each other out (the negative BSK in Fig. 6 is also supporting evidence). The sensitivity of these sub-components to the horizontal resolution is further analyzed separately in the following section.

#### d. Sensitivity to horizontal resolution (ROMS1 versus ROMS2)

Fig. 12 illustrates the different energy cycle quantities between ROMS2 (~0.5 km resolution) and ROMS1 (~1.5 km resolution). The increase of the reservoir of PKE from ROMS1 to ROMS2 is a matter of course as a deeper range of submesoscales are resolved by the ROMS2 simulation, but, surprisingly, the production of kinetic energy via BSK is reduced in the ROMS2 simulation. To obtain a more insightful understanding of the sensitivity of submesoscale energetics to horizontal resolution, we decompose BSK into six terms,

$$BSK_1 = -\rho_0 \overline{u'u'} \frac{\partial \bar{u}}{\partial x}, \quad (16)$$

$$BSK_2 = -\rho_0 \overline{v'v'} \frac{\partial \bar{v}}{\partial y}, \quad (17)$$

$$BSK_3 = -\rho_0 \overline{u'v'} \frac{\partial \bar{u}}{\partial y}, \quad (18)$$

$$BSK_4 = -\rho_0 \overline{v'u'} \frac{\partial \bar{v}}{\partial y}, \quad (19)$$

$$BSK_5 = -\rho_0 \overline{u'w'} \frac{\partial \bar{u}}{\partial z}, \text{ and} \quad (20)$$

$$BSK_6 = -\rho_0 \overline{v'w'} \frac{\partial \bar{v}}{\partial z}, \quad (21)$$

where  $BSK_1$  and  $BSK_2$  are the contribution of diagonal horizontal Reynolds stress components, i.e., normal stresses (HRS),  $BSK_3$  and  $BSK_4$  are the torsional horizontal shear production (HSP), and  $BSK_5$  and  $BSK_6$  are the vertical shear production (VSP). Fig. 13 compares the averaged energy terms ( $BSK_1$ ,  $BSK_2$ ,  $BSK_3$ ,  $BSK_4$ ,  $BSK_5$ , and  $BSK_6$ ) between the ROMS1 and ROMS2 simulation. Among these terms, The  $BSK_2$  (meridional normal

Reynolds stress) and BSK<sub>4</sub> (horizontal shear production from stresses associated with the meridional mean flow) turn out to be negative and tend to cancel the others. As such, the net BSK results from a competition between inverse (negative BSK) and forward (positive BSK) energy transfers. Indeed, in the ROMS2 simulation, each energy term is actually enhanced in magnitude while the overall net effect changes less (Fig. 13). The remarkable negative increase of BSK<sub>2</sub> and BSK<sub>4</sub> from ROMS1 to ROMS2 leads to the smaller BSK in the ROMS2 simulation.

In Fig. 14, the vertical profiles of the root-mean-square (RMS) values for each term are compared between the two simulations. The results show that the HRS and HSP are extremely active in the surface boundary layer, whereas the VSP peaks in the middle of the mixed layer, resembling the baroclinic production of submesoscale kinetic energy consistent with mixed layer vertical structures that extract and interact with multiple sources of energy (e.g., Haney et al. 2015). Ratios of RMS values between the ROMS1 and ROMS2 simulation help assess the sensitivity to the horizontal resolution (e.g.,  $R = HSP_{MR\_RMS} / HSP_{HR\_RMS}$ , a smaller ratio means greater sensitivity). Fig. 14d shows that VSP (the orange line) is most sensitive to the horizontal resolution, more so than HRS and HSP (purple and yellow lines) as a consequence of the enhanced submesoscale vertical velocity in ROMS2. At higher resolution, a nonhydrostatic model will become required as boundary layer turbulence becomes permitted when the horizontal grid rivals the boundary layer depth (Hamlington et al. 2014).

#### *e. Scale-dependent energy budget*

Submesoscale instabilities arise from a variety of mechanisms depending on the flow conditions: the barotropic shear production from the background flow dominates the production of SMKE in the tropical ocean study of Wang et al. (2018), whereas here baroclinic transfers from SMPE dominate. The mechanisms of this downscale transfer via BSK, consisting of the effects of normal strain and flow shear, deserve more detailed analysis. Fig. 12 shows that the quantification of energy production remains sensitive to the horizontal resolution of numerical simulations, even at the high resolutions used here (~0.5 km and ~1.5 km). This is because some submesoscales, for example, slantwise symmetric instabilities, are only partly resolved, extract geostrophic kinetic energy, and give rise to downscale energy cascades (Taylor and Ferrari 2010; Thomas et al. 2013). The effects of SI are highly sensitive to resolution (Bachman and Taylor 2014).

BSK and PKE are the major SMKE production terms of the barotropic and baroclinic routes for forward energy transfers. In the barotropic modes, although a net downscale energy transfer by BSK is confirmed, the energy conversions in Fig. 12 highly depend on the cut-off scale defining the submesoscales. Here we revisit whether there is a sharp upper bound of the submesoscale (20 km) relevant to energy transfers via spectral SMKE generation:

$$E_{BSK}(k) = \Re \left[ -\left( \mathbf{u}'_h{}^* \cdot (\bar{\mathbf{u}}_h \cdot \nabla) \mathbf{u}'_h \right) - \mathbf{u}'_h{}^* \cdot (\mathbf{u}' \cdot \nabla) \bar{\mathbf{u}}_h - \mathbf{u}'_h{}^* \cdot (\bar{\mathbf{u}} \cdot \nabla) \bar{\mathbf{u}}_h \right], \quad (22)$$

$$E_{PKE}(k) = \Re \left[ -\frac{g}{\rho_0} w'^* \rho' \right], \quad (23)$$

$$E_{PW}(k) = \Re \left[ -\frac{1}{\rho_0} \mathbf{u}'_h{}^* \cdot \nabla p' \right], \quad (24)$$

$$E_{ADK}(k) = \Re \left[ -\mathbf{u}'_h{}^* \cdot (\mathbf{u}'_h \cdot \nabla) \mathbf{u}'_h - \mathbf{u}'_h{}^* \cdot w' \frac{\partial \mathbf{u}'_h}{\partial z} \right], \quad (25)$$

where  $\nabla_h$  is the horizontal divergence operator,  $\Re$  is the symbol of the real part, and  $*$  is the complex conjugate. In this way, scale-dependent energy budgets can be estimated.

Fig. 15 shows the spectral energy budget averaged over the upper 50 m. The PKE exhibits a dominant positive energy budget with a peak at a wavelength of  $\sim 15$  km, where BSK reaches its negative maximum. With the decrease in the length scale, the BSK increases continuously and experiences a transition to positive (forward) values at  $\sim 10$  km. The BSK has contrary impacts on the energy cascade above or below the transition scale. The negative peak of BSK is likely associated with the barotropized submesoscale energy from PKE that subsequently enters an inverse energy cascade (Callies et al. 2016; Schubert et al. 2020). This is attributed to the negative sub-components of BSK shown in Figure 13. A similar upscale energy transfer for submesoscale eddies in the upper ocean of the Agulhas Current system was recently reported (Schubert et al. 2020). Alternatively, it is defined as the submesoscale balanced KE (Torres et al. 2018) that tends to enter larger scales. Note that this is generated by the local submesoscale processes, distinct from the aforementioned SBK arising from the boundary effects. The positive peak of BSK occurs at wavelengths smaller than 10 km, consistent with the result of the divergence spectrum observed in Fig. 5. Hence, it is fair to infer that the divergence of flow could be a more typical feature for unbalanced submesoscale processes that can drive forward KE cascade at smaller submesoscales. Using the geostrophic

unbalance to isolate the submesoscale range is dynamically meaningful in understanding that on these scales the submesoscale is quite unlike the mesoscale in Rossby number and horizontal divergence, so a downscale cascade of KE is one result. As such, the scale partition is critical for estimating the energy transfer between scales. As in this case, a decrease of the upper boundary will increase the BSK but reduce the PKE. A wavelength of 10 km seems to be critical if unbalanced submesoscale motions are of primary interest. As estimated in Section 3 that about ten times the grid spacing is required to well resolve a motion at a certain wavelength, the grid size for this case should be no larger than 1 km to evaluate the forward energy cascade correctly.

*f. Scale-dependence of transfers of KE and buoyancy production*

A final consequence of the energy budget gives rise to the net injection or sink of kinetic and potential energy as functions of the length scale. The spectral KE flux can be defined as

$$\Pi_1(k) = -\int_k^{k_{\max}} E(k) dk, \quad (26)$$

where  $E(k) = \Re(\mathbf{u}_h^* \cdot (\mathbf{u}_h \cdot \nabla) \mathbf{u}_h)$ . Thus, the sign (negative or positive) of the flux implies the directions (inverse or forward) of the total KE cascade from larger to smaller scales (Scott and Wang 2005; Scott and Arbic 2007). Fig. 16a shows the depth-dependent spectral KE flux in the upper ocean. The energy flux of KE tends to be upscale (negative) cascade at mesoscales above the transition scale (divided by the black line in Fig. 16a). The forward cascade (red shading in Fig. 16a) mainly occurs in the upper mixed layer, which is highly consistent with the vertical distribution of the BSK rather than the PKE (recall Fig.7). The transition scale is  $\sim 25$  km for the near-surface layer and quickly decreases to  $\sim 10$  km in the middle of the mixed layer. In the main thermocline, the forward KE energy flux is dramatically reduced but still displays a slight forward energy cascade at scales less than 10 km.

Likewise, the spectral buoyancy flux can be defined as

$$\Pi_2(k) = \int_k^{k_{\max}} \Re(w^* \hat{b}) dk. \quad (27)$$

As shown in Fig. 16b, the buoyancy flux in the upper ocean is mostly positive, implying a continuous downscale cascade of the potential energy across the scales. The enhancement of the flux at  $\sim 100$  km is likely associated with the generation of mesoscale eddies. In the

submesoscale range, the buoyancy flux mainly exists within the mixed layer, consistent with the vertical distribution of PKE observed in Fig. 7b. The conversion of PE to KE serves as an important energy sink for the PE in the mesoscale energy cycle (Ferrari and Wunsch 2009) and is seemingly similar for the submesoscale found in this study. Note that the buoyancy flux in the mixed layer becomes much smaller at  $\sim 10$  km, indicative of weaker baroclinic effects at high wavenumbers in Fig. 16b (which agrees with the quick decrease of PKE at high wavenumbers in Fig. 15).

## 5. Summary

Submesoscale activities in the upper ocean act as a dynamical conduit between the mesoscale and the dissipation scale by providing substantial available potential energy and driving an effective forward kinetic and potential energy cascade. This work uses high-resolution simulations to investigate the submesoscale energetics in the upper ocean of the Kuroshio Extension region, with a focus on downscale energy transfers. It was found that both submesoscale kinetic and potential energy (SMKE and SMPE) play a significant role in converting energy to smaller scales through surface-trapped submesoscale modes. A large amount of submesoscale available potential energy is generated by stirring the heterogeneous surface buoyancy field, which is subsequently converted to submesoscale eddies through buoyancy production (as in Capet et al. 2016). Further analysis of the submesoscale energetics reveals that

- The frequency–wavenumber spectrum analysis identifies a broad-banded enhanced vertical vorticity and especially horizontal divergence in the high-frequency, high-wavenumber space, which are taken as the defining characteristics of geostrophically unbalanced submesoscale flows. This spectral characterization is distinct from that of narrow-banded inertial-gravity waves in frequency–wavenumber space.
- Submesoscale kinetic energy is generated mainly in the mixed layer by extracting energy from the mean flow. Both barotropic and baroclinic routes (BKE $\rightarrow$ SMKE and BPE $\rightarrow$ SMPE $\rightarrow$ SMKE) efficiently contribute to the generation of submesoscale phenomena.
- Shear production is particularly active in the near-surface layer and drives a forward energy cascade at the smaller submesoscales (i.e., unbalanced submesoscales); while baroclinic conversion of potential into kinetic energy dominates the middle mixed layer

601 and generates submesoscale eddies. Some of the energy in these eddies subsequently  
602 enters an inverse KE cascade toward the larger submesoscales.

- 603 • Transfer of kinetic energy from the background to the submesoscales effectively  
604 contributes to a net forward (positive) KE transfer, although this contribution is an  
605 amalgam of normal Reynolds shear stress production (HRS), torsional Reynolds shear  
606 stress production (HSP), and vertical Reynolds shear stress production (VSP), which tend  
607 to cancel each other during eddy-mean interaction. All of these contributions are  
608 differently sensitive to horizontal resolution ( $\sim 1.5$  km versus  $\sim 0.5$  km). VSP is the most  
609 sensitive term, although it is the least significant component for the generation of SMKE  
610 at these resolutions.
- 611 • The KE and PE transfers from the outer domains provide a significant portion of energy  
612 budget—indeed, the KE flux from the outer domains is the largest term in the entire  
613 budget. Care is needed to understand this term together with the transfers between the  
614 background and submesoscale. In the approach chosen here, the boundary term energizes  
615 the background kinetic energy and then some of this energy is transferred downscale to  
616 the submesoscale. An alternative, equally legitimate framing (APPENDIX) places the  
617 boundary flow of KE first in the submesoscale, which then cascades upscale to the  
618 background flow. It is critically important in regional calculations to consider and  
619 understand that energy fluxes across scales can be contradictory in direction when such  
620 boundary terms are important as they are for KE here.

621 In this study, we mainly focused on the energy transfer routes by submesoscale processes  
622 in the upper ocean of the Kuroshio Extension region. A key finding is a method for  
623 identifying the scales dominated by submesoscale turbulence, which are distinct from the  
624 scales of submesoscale instabilities. Once identified, the next key point revealed is that the  
625 net forward energy transfers occur at scales that are small when compared to those of the  
626 mixed layer baroclinic instabilities. Seasonal variability of submesoscales is not discussed but  
627 it affects submesoscale processes by changing atmospheric forcing and background flow  
628 (Sasaki et al. 2014; Qiu et al. 2014; Rocha et al. 2016). Submesoscale processes should be  
629 enhanced as a response to the intensified atmospheric forcing in winter, although managing  
630 model and observation resolution consistently across seasons is an issue (Dong et al. 2020a).  
631 Energy pathways are similar across seasons, but their small changes can be revealing of the  
632 charging and discharging of different reservoirs (Dong et al. 2020b). Further studies of  
633 higher-resolution simulation and field observations are required to figure out the energetic

634 details of submesoscale effects throughout the world ocean, over the seasons, and over future  
635 climates.

636

637 *Acknowledgments.*

638 The authors would like to thank NASA (<http://oceancolor.gsfc.nasa.gov>) for the MODIS-  
639 Aqua data and the QuikSCAT forcing (<http://podaac.jpl.nasa.gov>), NOAA ICOADS  
640 (<http://icoads.noaa.gov>) and SODA (<https://www2.atmos.umd.edu/~ocean/>) were also part of  
641 the forcing data. The data of US KESS project  
642 (<https://uskes.whoi.edu/overview/dataproducts/>) were used to validate the velocity field in  
643 the simulation. This study is supported by the National Natural Science Foundation of China  
644 (51709092, 41776040). Haijin Cao is also partly supported by the Natural Science  
645 Foundation of Jiangsu Province (BK20170865) and by the National Key Research and  
646 Development Program of China grant (2017YFA0604104). Baylor Fox-Kemper is supported  
647 in part by NSF 1350795 and in part by NOAA NA19OAR4310366. Zhiyou Jing is supported  
648 by Chinese Academy of Sciences (ZDBS-LY-DQC011, ISEE2018PY05).

649

650 *Data Availability Statement.*

651 Source data for ROMS simulations are available at scientific database of South China Sea  
652 Institute of Oceanology ([www.scsio.csdb.cn](http://www.scsio.csdb.cn)).

653

654 APPENDIX

## 655 **Energy budget equations**

656 With the above-mentioned energy definitions (Fig. 2), the energy budget equations with  
657 boundary terms for a fixed ocean domain are as follows. The BKE equation is expressed as

$$\begin{aligned}
\frac{\partial}{\partial t}(\text{BKE}) = & \underbrace{-\nabla \cdot [\bar{\mathbf{u}}(\text{BKE})]}_{\text{ADK}_1} + \text{BndyKE} \\
& \underbrace{-\rho_0(u'\mathbf{u} \cdot \nabla \bar{\mathbf{u}} + v'\mathbf{u}' \cdot \nabla \bar{\mathbf{v}})}_{-\text{BSK}} \underbrace{-\nabla \cdot (\bar{\mathbf{u}}\bar{\mathbf{p}})}_{\text{PW}_1} \underbrace{-\overline{g\rho'w}}_{\text{PKE}_1} + \overline{D_{K1}} + \overline{F_{K1}}, \quad (\text{A1})
\end{aligned}$$

where the subscript 1 denotes the larger, slower scales. Then, the SMKE equation becomes

$$\begin{aligned}
\frac{\partial}{\partial t}(\text{SMKE}) = & \underbrace{-\frac{1}{2}\rho_0\nabla \cdot [\mathbf{u}(u'^2 + v'^2)]}_{\text{ADK}_2} \underbrace{-\nabla \cdot (\mathbf{u}'\bar{p})}_{\text{PW}_2} \\
& \underbrace{-\overline{g\rho'w'}}_{\text{PKE}_2} \underbrace{-\rho_0(u'\mathbf{u}' \cdot \nabla \bar{\mathbf{u}} + v'\mathbf{u}' \cdot \nabla \bar{\mathbf{v}})}_{\text{BSK}} + \overline{D_{K2}} + \overline{F_{K2}}, \quad (\text{A2})
\end{aligned}$$

where the subscript 2 denotes the submesoscale. Note that the energy leakage or source (BndyKE) works on the BKE budget in this formulation, and then BSK transfers energy from the BKE to the SMKE. However, SBK is the difference between BndyKE and BSK in Eq. (A1), so it is equally legitimate to consider the BndyKE as acting on the SMKE budget and then SBK is the transfer term from the submesoscale to the background. Thus, in Figs. 2 and 12, we illustrate the BndyKE term as arriving between the SMKE and BKE reservoirs. The expression of SBK is shown in Eq. 13.

Similarly, the energy equations for BPE and SMPE can be

$$\frac{\partial}{\partial t}(\text{BPE}) = \underbrace{-\nabla \cdot [\bar{\mathbf{u}}(\text{BPE})]}_{\text{ADP}_1} \underbrace{+\overline{g\rho'w}}_{-\text{PKE}_1} + \text{BndyPE} + \underbrace{\frac{g^2}{\rho_0 N^2} \overline{\rho'\mathbf{u}' \cdot \nabla \bar{\rho}}}_{-\text{BSP}} + \overline{D_{P1}} + \overline{F_{P1}}, \quad (\text{A3})$$

$$\frac{\partial}{\partial t}(\text{SMPE}) = \underbrace{-\nabla \cdot \left[ \mathbf{u} \left( \frac{g^2 \rho'^2}{2\rho_0 N^2} \right) \right]}_{\text{ADP}_2} \underbrace{-\frac{g^2}{\rho_0 N^2} \overline{\rho'\mathbf{u}' \cdot \nabla \bar{\rho}}}_{\text{BSP}} \underbrace{+\overline{g\rho'w'}}_{-\text{PKE}_2} + \overline{D_{P2}} + \overline{F_{P2}}. \quad (\text{A4})$$

The integrals of the boundary terms are

$$\int_V (\text{BSK} + \text{SBK}) dV = \int_V -\rho_0 \nabla_i (\bar{u}_j u'_j u'_i) dV = \oint_S -\rho_0 (\bar{u}_j u'_j u'_i) n_i dS, \quad (\text{A5})$$

$$\int_V (\text{BSP} + \text{SBP}) dV = \int_V -\frac{g^2}{\rho_0 N^2} \nabla_i \cdot (\bar{u}'_i \rho' \bar{\rho}) dV = \oint_S -\frac{g^2}{\rho_0 N^2} (\bar{u}'_i \rho' \bar{\rho}) n_i dS, \quad (\text{A6})$$

where the repeated indices indicate sums over i, j in all the directions (Einstein summation) and  $n_i$  is the outward normal vector component in the i direction. Note that the last form on the right always depends on a velocity oriented along the outward normal, thus global



677 integrals bounded by basin boundaries will be zero. For a fixed ocean domain with open  
678 boundaries, the normal velocities are not zero (right-hand-sides of Eqs. A5 and A6), and  
679 serves to exchange energy from (to) outer domains. The boundary terms can provide  
680 important energy source or leakage for the research domain as they do in this study.

681

## 682 REFERENCES

683 Aiki, H., and K. J. Richards, 2008: Energetics of the global ocean: The role of layer-thickness  
684 form drag. *J. Phys. Oceanogr.*, **38**, 1845–1869, <https://doi.org/10.1175/2008JPO3820.1>.

685 Arbic, B.K., M., Müller, J.G., Richman, J.F., Shriver, A.J., Morten, R.B., Scott, G. Sérazin,  
686 and T., Penduff, 2014: Geostrophic turbulence in the frequency–wavenumber domain:  
687 Eddy-driven low-frequency variability. *J. Phys. Oceanogr.*, **44**(8), 2050–2069,  
688 <https://doi.org/10.1175/JPO-D-13-054.1>.

689 Bachman S., and B. Fox-Kemper, 2013: Eddy parameterization challenge suite. I: Eady  
690 spindown. *Ocean Modell.*, **64**, 12–28, <http://dx.doi.org/10.1016/j.ocemod.2012.12.003>.

691 Bachman, S. D., B. Fox-Kemper, J. Taylor, and L. Thomas, 2017a: Parameterization of  
692 frontal symmetric instabilities. I: Theory for resolved fronts. *Ocean Modell.*, **109**, 72–95,  
693 <https://doi.org/10.1016/j.ocemod.2016.12.003>.

694 —, J. Taylor, K. Adams, and P. Hosegood, 2017b: Mesoscale and submesoscale effects on  
695 mixed layer depth in the Southern Ocean. *J. Phys. Oceanogr.*, **47**, 2173–2188,  
696 <https://doi.org/10.1175/JPO-D-17-0034.1>.

697 —, and J. R. Taylor, 2014: Modelling of partially-resolved oceanic symmetric  
698 instability. *Ocean Modell.*, **82**, 15–27, <https://doi.org/10.1016/j.ocemod.2014.07.006>.

699 Boccaletti, G., R. Ferrari, and B. Fox-Kemper, 2007: Mixed layer instabilities and  
700 restratification. *J. Phys. Oceanogr.*, **37**, 2228–2250, <http://doi:10.1175/JPO3101.1>.

701 Buckingham, C., A. N. Garabato, A. Thompson, L. Brannigan, A. Lazar, D. Marshall, A. J. G.  
 702 Nurder, G. Damerell, K. Heywood, and S. Belcher, 2016: Seasonality of submesoscale  
 703 flows in the ocean surface boundary layer. *Geophys. Res. Lett.*, **43**, 2118–2126,  
 704 <https://doi.org/10.1002/2016GL068009>.

705 Buckingham, C., Z. Khaleel, A. Lazar, A. Martin, J. Allen, A. N. Garabato, A. Thompson,  
 706 and C. Vic, 2017: Testing Munk's hypothesis for submesoscale eddy generation using  
 707 observations in the North Atlantic. *J. Geophys. Res. Oceans*, **122**: 6725–6745,  
 708 <https://doi.org/10.1002/2017JC012910>.

709 Brannigan, L., D. Marshall, A. N. Garabato, A. J. G. Nurser, and J. Kaiser, 2017:  
 710 Submesoscale instabilities in mesoscale eddies. *J. Phys. Oceanogr.*, **47**, 3061–3085,  
 711 <https://doi.org/10.1175/JPO-D-16-0178.1>.

712 Cao, H., Z. Jing, B. Fox-kemper, T. Yan, and Y. Qi, 2019: Scale transition from geostrophic  
 713 motions to internal waves in the northern South China Sea. *J. Geophys. Res. Oceans*, **124**,  
 714 9364–9383, <https://doi.org/10.1029/2019JC015575>.

715 —, and Z. Jing, 2020: Submesoscale ageostrophic motions within and below the mixed layer  
 716 of the northwestern Pacific Ocean. Submitted to *J. Geophys. Res. Oceans*.

717 Callies, J., R. Ferrari, J. M. Klymak, and J. Gula, 2015: Seasonality in submesoscale  
 718 turbulence. *Nat. Commun.*, **6**, 6862, <https://doi.org/10.1038/ncomms7862>.

719 —, G. Flierl, R. Ferrari, and B. Fox-Kemper, 2016: The role of mixed-layer instabilities in  
 720 submesoscale turbulence. *J. Fluid Mech.*, **788**, 5–41,  
 721 <https://doi.org/10.1017/jfm.2015.700>.

722 Capet, X., J. McWilliams, M. Molemaker, and A. Shchepetkin, 2008a: Mesoscale to  
 723 submesoscale transition in the California Current system. Part III: Energy balance and  
 724 flux. *J. Phys. Oceanogr.*, **38**, 2256–2269, <https://doi.org/10.1175/2008JPO3810.1>.

725 —, J. McWilliams, M. Molemaker, and A. Shchepetkin, 2008b: Mesoscale to submesoscale  
 726 transition in the California Current system. Part I: Flow structure, eddy flux, and  
 727 observational tests. *J. Phys. Oceanogr.*, **38**, 29–43,  
 728 <https://doi.org/10.1175/2007JPO3671.1>.

729 —, G. Roullet, P. Klein, and G. Maze, 2016: Intensification of upper-ocean submesoscale  
 730 turbulence through Charney baroclinic instability. *J. Phys. Oceanogr.*, **46**, 3365–3384,  
 731 <https://doi.org/10.1175/JPO-D-16-0050.1>.

732 Carton, J., and B. Giese, 2008: A reanalysis of ocean climate using Simple Ocean Data  
 733 Assimilation (SODA). *Mon. Weather Rev.*, **136**, 2999–3017,  
 734 <https://doi.org/10.1175/2007MWR1978.1>.

735 Charney, J. G., 1971: Geostrophic turbulence. *J. Atmos. Sci.*, **28**, 1087–1095,  
 736 [https://doi.org/10.1175/1520-0469\(1971\)028<1087:GT>2.0.CO;2](https://doi.org/10.1175/1520-0469(1971)028<1087:GT>2.0.CO;2).

737 Chen, R., G. R. Flierl, and C. Wunsch, 2014: A description of local and nonlocal eddy-mean  
 738 flow interaction in a global eddy-permitting state estimate. *J. Phys. Oceanogr.*, **44**, 2336–  
 739 2352, <https://doi.org/10.1175/JPO-D-14-0009.1>.

740 Cronin, M., and D. Watts, 1996: Eddy-mean flow interaction in the Gulf Stream at 68°W.  
 741 Part I: Eddy energetics. *J. Phys. Oceanogr.*, **26**, 2107–2131, [https://doi.org/10.1175/1520-](https://doi.org/10.1175/1520-0485(1996)026<2107:EFHITG>2.0.CO;2)  
 742 [0485\(1996\)026<2107:EFHITG>2.0.CO;2](https://doi.org/10.1175/1520-0485(1996)026<2107:EFHITG>2.0.CO;2).

743 D'Asaro, E. A., D. F. Carlson, M. Chamecki, R. Harcourt, B. Haus, B. Fox-Kemper, M. J.  
 744 Molemaker, A. Poje, and D. Yang, 2020: Advances in observing and understanding  
 745 small-scale open ocean circulation during the GoMRI era. *Front. Mar. Sci.*, **7**, 349,  
 746 <https://doi.org/10.3389/fmars.2020.00349>.

747 —, C. Lee, L. Rainville, R. Harcourt, and L. Thomas, 2011: Enhanced turbulence and  
 748 energy dissipation at ocean fronts. *Science*, **332**, 318–322,  
 749 <https://doi.org/10.1126/science.1201515>.

750 —, A. Y., Shcherbina, J. M., Klymak, J., Molemaker, G., Novelli, C. M., Guigand, A. C.,  
 751 Haza, B. K., Haus, E. H., Ryan, G.A., Jacobs, and H.S., Huntley, 2018: Ocean  
 752 convergence and the dispersion of flotsam. *P. Natl. Acad. Sci. USA*, **115**(6), 1162–1167,  
 753 <https://doi.org/10.1073/pnas.1718453115>.

754

755 de Boyer Montégut, C., G. Madec, A. Fischer, A. Lazar, and D. Iudicone, 2004: Mixed layer  
 756 depth over the global ocean: An examination of profile data and a profile-based  
 757 climatology. *J. Geophys. Res. Oceans*, **109**, C12003,  
 758 <https://doi.org/10.1029/2004JC002378>.

759 Dong, J., B. Fox-Kemper, H. Zhang, and C. Dong, 2020a: The size of submesoscale  
 760 baroclinic instability globally. *J. Phys. Oceanogr.*, **50**, 2649–2667,  
 761 <https://doi.org/10.1175/JPO-D-20-0043.1>.

762 —, B. Fox-Kemper, H. Zhang, and C. Dong, 2020b: The seasonality of submesoscale energy  
 763 production, content, and cascade. *Geophys. Res. Lett.*, **47**,  
 764 <http://dx.doi.org/10.1029/2020GL087388>

765 du Plessis, M., S. Swart, I. J. Ansorge, A. Mahadevan, and A. F. Thompson, 2019: Southern  
 766 ocean seasonal restratification delayed by submesoscale wind-front interactions. *J. Phys.*  
 767 *Oceanogr.*, **49**, 1035–1053, <https://doi.org/10.1175/JPO-D-18-0136.1>.

768 Ferrari, R., and C. Wunsch, 2009: Ocean circulation kinetic energy: reservoirs, sources, and  
 769 sinks. *Annu. Rev. Fluid Mech.*, **41**, 253–282.  
 770 <https://doi.org/10.1146/annurev.fluid.40.111406.102139>.

771 Fox-Kemper, B., R. Ferrari, and R. Hallberg, 2008: Parameterization of mixed layer eddies.  
 772 Part I: Theory and diagnosis. *J. Phys. Oceanogr.*, **38**, 1145–1165,  
 773 <https://doi.org/10.1175/2007JPO3792.1>

774 Gent, P., and J. McWilliams, 1990: Isopycnal mixing in ocean circulation models. *J. Phys.*  
 775 *Oceanogr.*, **20**, 150–155, [https://doi.org/10.1175/1520-](https://doi.org/10.1175/1520-0485(1990)020<0150:IMIOCM>2.0.CO;2)  
 776 [0485\(1990\)020<0150:IMIOCM>2.0.CO;2](https://doi.org/10.1175/1520-0485(1990)020<0150:IMIOCM>2.0.CO;2).

777 Gentemann, C. L., J. P. Scott, P. L. F. Mazzini, C. Pianca, S. Akella, P. J. Minnett,  
 778 P. Cornillon, B. Fox-Kemper, I. Cetinic, T. M. Chin, J. Gomez-Valdes, J. Vazquez-  
 779 Cuervo, V. Tsonos, L. Yu, R. Jenkins, S. D. Halleux, D. Peacock, and N. Cohen, 2020:  
 780 Saildrone: adaptively sampling the marine environment. *B. Am. Meteorol. Soc.*, **101**,  
 781 E744-E762, <https://doi.org/10.1175/BAMS-D-19-0015.1>.

782 Gill, A., 1982: *Atmosphere-Ocean Dynamics*. Academic Press, 662 pp.

783 Grooms, I., L. Nadeau, and K. Smith, 2013: Mesoscale eddy energy locality in an idealized  
 784 ocean model. *J. Phys. Oceanogr.*, **43**, 1911–1923, [https://doi.org/10.1175/JPO-D-13-](https://doi.org/10.1175/JPO-D-13-036.1)  
 785 [036.1](https://doi.org/10.1175/JPO-D-13-036.1).

786 Gula, J., M. Molemaker, and J. McWilliams, 2014: Submesoscale cold filaments in the Gulf  
 787 Stream. *J. Phys. Oceanogr.*, **44**, 2617–2643, <https://doi.org/10.1175/JPO-D-14-0029.1>.

788 Hamlington, P. E., L. P. Van Roekel, B. Fox-Kemper, K. Julien, and G. P. Chini, 2014:  
 789 Langmuir-submesoscale interactions: Descriptive analysis of multiscale frontal spindown  
 790 simulations. *J. Phys. Oceanogr.*, **44**, 2249–2272, [https://doi.org/10.1175/JPO-D-13-](https://doi.org/10.1175/JPO-D-13-0139.1)  
 791 [0139.1](https://doi.org/10.1175/JPO-D-13-0139.1).

792 Haney, S., B. Fox-Kemper, K. Julien, and A. Webb, 2015: Symmetric and geostrophic  
 793 instabilities in the wave-forced ocean mixed layer. *J. Phys. Oceanogr.*, **45**, 3033–3056,  
 794 <https://doi.org/10.1175/JPO-D-15-0044.1>.

795 Hoskins, B. J., 1974: The role of potential vorticity in symmetric stability and  
 796 instability. *Quart. J. Roy. Meteor. Soc.*, **100**, 480–482,  
 797 <https://doi.org/10.1002/qj.49710042520>.  
 798  
 799 Huang, R. X., 1999: Mixing and energetics of the oceanic thermohaline circulation. *J. Phys.*  
 800 *Oceanogr.*, **29**, 727–746, [https://doi.org/10.1175/1520-](https://doi.org/10.1175/1520-0485(1999)029<0727:MAEOTO>2.0.CO;2)  
 801 [0485\(1999\)029<0727:MAEOTO>2.0.CO;2](https://doi.org/10.1175/1520-0485(1999)029<0727:MAEOTO>2.0.CO;2).  
 802 Jing, Z., Y. Qi, B. Fox-Kemper, Y. Du, and S. Lian, 2016: Seasonal thermal fronts and their  
 803 associations with monsoon forcing on the continental shelf of northern South China Sea:  
 804 Satellite measurements and three repeated field surveys in winter, spring and summer. *J.*  
 805 *Geophys. Res. Oceans*, **121**, 1914–1930, <https://doi.org/10.1002/2015JC011222>.  
 806 —, B. Fox-Kemper, H. Cao, R. Zheng, and Y. Du, 2020: Submesoscale Density Fronts and  
 807 their Dynamical Impacts on the Eddy-active Northwest Pacific Subtropical Ocean.  
 808 Submitted to *J. Phys. Oceanogr.*  
 809 Kang, D., and E. N. Curchitser, 2015: Energetics of eddy-mean flow interactions in the Gulf  
 810 Stream region. *J. Phys. Oceanogr.*, **45**, 1103–1120, [https://doi.org/10.1175/JPO-D-14-](https://doi.org/10.1175/JPO-D-14-0200.1)  
 811 [0200.1](https://doi.org/10.1175/JPO-D-14-0200.1).  
 812 —, and O. B. Fringer, 2010: On the calculation of available potential energy in internal wave  
 813 fields. *J. Phys. Oceanogr.*, **40**, 2539–2545, <https://doi.org/10.1175/2010JPO4497.1>.  
 814 Klein, P., B. L. Hua, G. Lapeyre, X. Capet, S. Le Gentil, and H. Sasaki, 2008: Upper ocean  
 815 turbulence from high-resolution 3D simulations. *J. Phys. Oceanogr.*, **38**, 1748–1763,  
 816 <https://doi.org/10.1175/2007JPO3773.1>.  
 817 Kraichnan, R. H., 1967: Inertial ranges in two-dimensional turbulence, *Phys. Fluids*, **16**,  
 818 1417–1423, <https://doi.org/10.1063/1.1762301>.

819 Lapeyre, G., and P. Klein, 2006: Dynamics of the upper oceanic layers in terms of surface  
820 quasigeostrophy theory. *J. Phys. Oceanogr.*, **36**, 165–176,  
821 <https://doi.org/10.1175/JPO2840.1>.

822 Large, W., J. McWilliams, and S. Doney, 1994: Oceanic vertical mixing: A review and a  
823 model with a nonlocal boundary layer parameterization. *Rev. Geophys.*, **32**, 363–403,  
824 <https://doi.org/10.1029/94RG01872>.

825 Lévy, M., P. Klein, and A. Tréguier, 2001: Impact of sub-mesoscale physics on production  
826 and subduction of phytoplankton in an oligotrophic regime. *J. Mar. Res.*, **59**, 535–565,  
827 <https://doi.org/10.1357/002224001762842181>.

828 —, D. Iovino, L. Resplandy, P. Klein, G. Madec, A. Tréguier, S. Masson, and K. Takahashi,  
829 2012: Large-scale impacts of submesoscale dynamics on phytoplankton: Local and  
830 remote effects. *Ocean Modell.*, **43–44**, 77–93,  
831 <https://doi.org/10.1016/j.ocemod.2011.12.003>.

832 Lorenz, E. N., 1955: Available potential energy and the maintenance of the general  
833 circulation. *Tellus*, **7**, 157–167, <https://doi.org/10.1111/j.2153-3490.1955.tb01148.x>.

834 Mahadevan, A., and A. Tandon, 2006: An analysis of mechanisms for submesoscale vertical  
835 motion at ocean fronts. *Ocean Modell.*, **14**, 241–256,  
836 <https://doi.org/10.1016/j.ocemod.2006.05.006>.

837 Molemaker, M., J. McWilliams, and X. Capet, 2010: Balanced and unbalanced routes to  
838 dissipation in an equilibrated Eady flow. *J. Fluid Mech.*, **654**, 35–63,  
839 <https://doi.org/10.1017/S0022112009993272>.

840 McWilliams, J., 2016. Submesoscale currents in the ocean. *Proc. R. Soc. A*, **472**, 20160117,  
841 <https://doi.org/10.1098/rspa.2016.0117>.

842 Munk, W., L. Armi, K. Fischer, and F. Zachariasen, 2000: Spirals on the sea, *Proc. R. Soc. A*,  
843 **456**, 1217–1280, <https://doi.org/10.1098/rspa.2000.0560>.

844

845 Nakamura, H., and A. Kazmin, 2003: Decadal changes in the North Pacific oceanic frontal  
846 zones as revealed in ship and satellite observations. *J. Geophys. Res. Oceans*, **108**, 3078,  
847 <https://doi.org/10.1029/1999JC000085>.

848 Pearson, B., B. Fox-Kemper, S. D. Bachman, and F. O. Bryan, 2017: Evaluation of scale-  
849 aware subgrid mesoscale eddy models in a global eddy-rich model. *Ocean Modell.*, **115**,  
850 42–58, <https://doi.org/10.1016/j.ocemod.2017.05.007>.

851 —, and B. Fox-Kemper, 2018: Log-normal turbulence dissipation in global ocean  
852 models. *Phys. Rev. Lett.*, **120**, 094501, <https://doi.org/10.1103/PhysRevLett.120.094501>.

853 Pearson, J., B. Fox-Kemper, R. Barkan, J. Choi, A. Bracco, and J. C. McWilliams, 2019:  
854 Impacts of convergence on Lagrangian statistics in the Gulf of Mexico. *J. Phy. Oceanogr.*,  
855 **49**(3), 675–690, <http://dx.doi.org/10.1175/JPO-D-18-0029.1>.

856 —, B. Fox-Kemper, B. Pearson, H. Chang, B. K. Haus, J. Horstmann, H. S. Huntley, A. D.  
857 Kirwan, Jr., B. Lund, and A. Poje, 2020: Biases in structure functions from observations  
858 of submesoscale flows. *J. Geophys. Res. Oceans*, **125**,  
859 <http://dx.doi.org/10.1029/2019JC015769>.

860 Plumb, R.A., 1983: A new look at the energy cycle. *J. Atmos. Sci.*, **40**, 1669–1688,  
861 [https://doi.org/10.1175/1520-0469\(1983\)040<1669:ANLATE>2.0.CO;2](https://doi.org/10.1175/1520-0469(1983)040<1669:ANLATE>2.0.CO;2).

862 Qiu B., K. Kelly, and T. Joyce, 1991: Mean flow and variability in the Kuroshio Extension  
863 from Geosat altimetry data. *J. Geophys. Res. Oceans*, **96**, 18491–18507,  
864 <https://doi.org/10.1029/91JC01834>.



865 —, 2000: Interannual variability of the Kuroshio Extension system and its impact on the  
866 wintertime SST field. *J. Phys. Oceanogr.*, **30**, 1486–1502, [https://doi.org/10.1175/1520-](https://doi.org/10.1175/1520-0485(2000)030,1486:IVOTKE.2.0.CO;2)  
867 0485(2000)030,1486:IVOTKE.2.0.CO;2.

868 —, and S. Chen, 2005: Variability of the Kuroshio Extension jet, recirculation gyre, and  
869 mesoscale eddies on decadal time scales. *J. Phys. Oceanogr.*, **35**, 2090–2103,  
870 <https://doi.org/10.1175/JPO2807.1>.

871 —, and S. Chen, 2010: Eddy-mean flow interaction in the decadally modulating Kuroshio  
872 Extension System. *Deep-Sea Res. II*, **57**, 1098–1110,  
873 <https://doi.org/10.1016/j.dsr2.2008.11.036>.

874 —, S. Chen, P. Klein, H. Sasaki, and Y. Sasai, 2014: Seasonal mesoscale and submesoscale  
875 eddy variability along the North Pacific Subtropical Countercurrent. *J. Phys. Oceanogr.*,  
876 **44**, 3079–3098, <https://doi.org/10.1175/JPO-D-14-0071.1>.

877 Rocha, C. B., S. Gille, T. Chereskin, and D. Menemenlis, 2016: Seasonality of submesoscale  
878 dynamics in the Kuroshio Extension. *Geophys. Res. Lett.*, **43**, 11304–11311,  
879 <https://doi.org/10.1002/2016GL071349>.

880 Rosso, I., A. Hogg, P. Strutton, A. Kiss, R. Matear, A. Klocker, and E. van Sebille, 2014:  
881 Vertical transport in the ocean due to submesoscale structures: Impacts in the Kerguelen  
882 region. *Ocean Modell.*, **80**, 10–23, <https://doi.org/10.1016/j.ocemod.2014.05.001>.

883 Rudnick, D. L., 2001: On the skewness of vorticity in the upper ocean. *Geophys. Res. Lett.*,  
884 **28**, 2045–2048, <https://doi.org/10.1029/2000GL012265>.

885 Saenz, J. A., Tailleux, R., Butler, E.D., Hughes, G.O. and Oliver, K.I., 2015: Estimating  
886 Lorenz’s reference state in an ocean with a nonlinear equation of state for seawater. *J.*  
887 *Phys. Oceanogr.*, **45**, 1242–1257, <https://doi.org/10.1175/JPO-D-14-0105.1>.

888 Schubert, R., J. Gula, R. J. Greatbatch, B. Baschek, and A. Biastoch, 2020: The submesoscale  
889 kinetic energy cascade: mesoscale absorption of submesoscale mixed layer eddies and  
890 frontal downscale fluxes. *J. Phys. Oceanogr.*, **50**, 2573–2589,  
891 <https://doi.org/10.1175/JPO-D-19-0311.1>.

892 Scott, R. B., and F. Wang, 2005: Direct evidence of an oceanic inverse kinetic energy  
893 cascade from satellite altimetry. *J. Phys. Oceanogr.*, **35**, 1650–1666,  
894 <http://doi:10.1175/JPO2771.1>.

895 —, and B. K. Arbic, 2007: Spectral energy fluxes in geostrophic turbulence: Implications for  
896 ocean energetics. *J. Phys. Oceanogr.*, **37**, 673–688, <https://doi.org/10.1175/JPO3027.1>.

897 Shchepetkin, A., and J. McWilliams, 2005: The regional oceanic modeling system (ROMS):  
898 a split-explicit, free-surface, topography-following-coordinate oceanic model. *Ocean*  
899 *Modell.*, **9**, 347–404, <https://doi.org/10.1016/j.ocemod.2004.08.002>.

900 Shcherbina, A., E. D'Asaro, C. Lee, J. Klymak, M. Molemaker, and J. McWilliams, 2013:  
901 Statistics of vertical vorticity, divergence, and strain in a developed submesoscale  
902 turbulence field. *Geophys. Res. Lett.*, **40**, 4706–4711, <https://doi.org/10.1002/grl.50919>.

903 Suzuki, N., Fox-Kemper, B., Hamlington, P.E. and Van Roekel, L.P., 2016: Surface waves  
904 affect frontogenesis. *J. Geophys. Res. Oceans*, **121**, 3597–3624,  
905 <https://doi.org/10.1002/2015JC011563>.

906 Tai, C., and W. White, 1990: Eddy variability in the Kuroshio Extension as revealed by  
907 Geosat altimetry: Energy propagation away from the jet, Reynolds stress, and seasonal  
908 cycle. *J. Phys. Oceanogr.*, **20**, 1761–1777, [https://doi.org/10.1175/1520-0485\(1990\)020,1761:EVITKE.2.0.CO;2](https://doi.org/10.1175/1520-0485(1990)020<1761:EVITKE.2.0.CO;2).

910 Thomas, L., A. Tandon, and A. Mahadevan, 2008: Submesoscale processes and dynamics.  
911 *Geophys. Monogr.*, **177**, 17–38, <https://doi.org/10.1029/177GM04>.

912

913 —, J. Taylor, R. Ferrari, and T. Joyce, 2013: Symmetric instability in the Gulf Stream.

914 *Deep-Sea Res. II*, **91**, 96–110, <https://doi.org/10.1016/j.dsr2.2013.02.025>.

915 Thompson, A., A. Lazar, C. Buckingham, A. Naveira Garabato, G. Damerell, and K.

916 Heywood, 2016: Open-ocean submesoscale motions: A full seasonal cycle of mixed layer

917 instabilities from gliders. *J. Phys. Oceanogr.*, **46**, 1285–1307,

918 <https://doi.org/10.1175/JPO-D-15-0170.1>.

919 Torres, H., P. Klein, D. Menemenlis, B. Qiu, Z. Su, J. Wang, S. Chen, and L. Fu, 2018:

920 Partitioning ocean motions into balanced motions and internal gravity waves: A modeling

921 study in anticipation of future space missions. *J. Geophys. Res. Oceans*, **123**, 8084–8105,

922 <https://doi.org/10.1029/2018JC014438>.

923 Tulloch, R., J. Marshall, and C. Hill, 2011: Scales, growth rates and spectral fluxes of

924 baroclinic instability in the ocean. *J. Phys. Oceanogr.*, **41**, 1057–1076,

925 <https://doi.org/10.1175/2011JPO4404.1>.

926 Villas Boas, A. B., F. Ardhuin, A. Ayet, M. A. Bourassa, P. Brandt, B. Chapron, B. D.

927 Cornuelle, J. T. Farrar, M. R. Fewings, B. Fox-Kemper, S. T. Gille, C. Gommenginger,

928 P. Heimbach, M. C. Hell, Q. Li, M. R. Mazloff, S. T. Merrifield, A. Mouche, M. H. Rio,

929 E. Rodriguez, J. D. Shutler, A. C. Subramanian, E. J. Terrill, M. Tsamados, C. Uebmann,

930 and E. van Sebille, 2019: Integrated observations and modeling of winds, currents, and

931 waves: requirements and challenges for the next decade. *Front. Mar. Sci.*, **6**, 425,

932 <http://doi.org/10.3389/fmars.2019.00425>

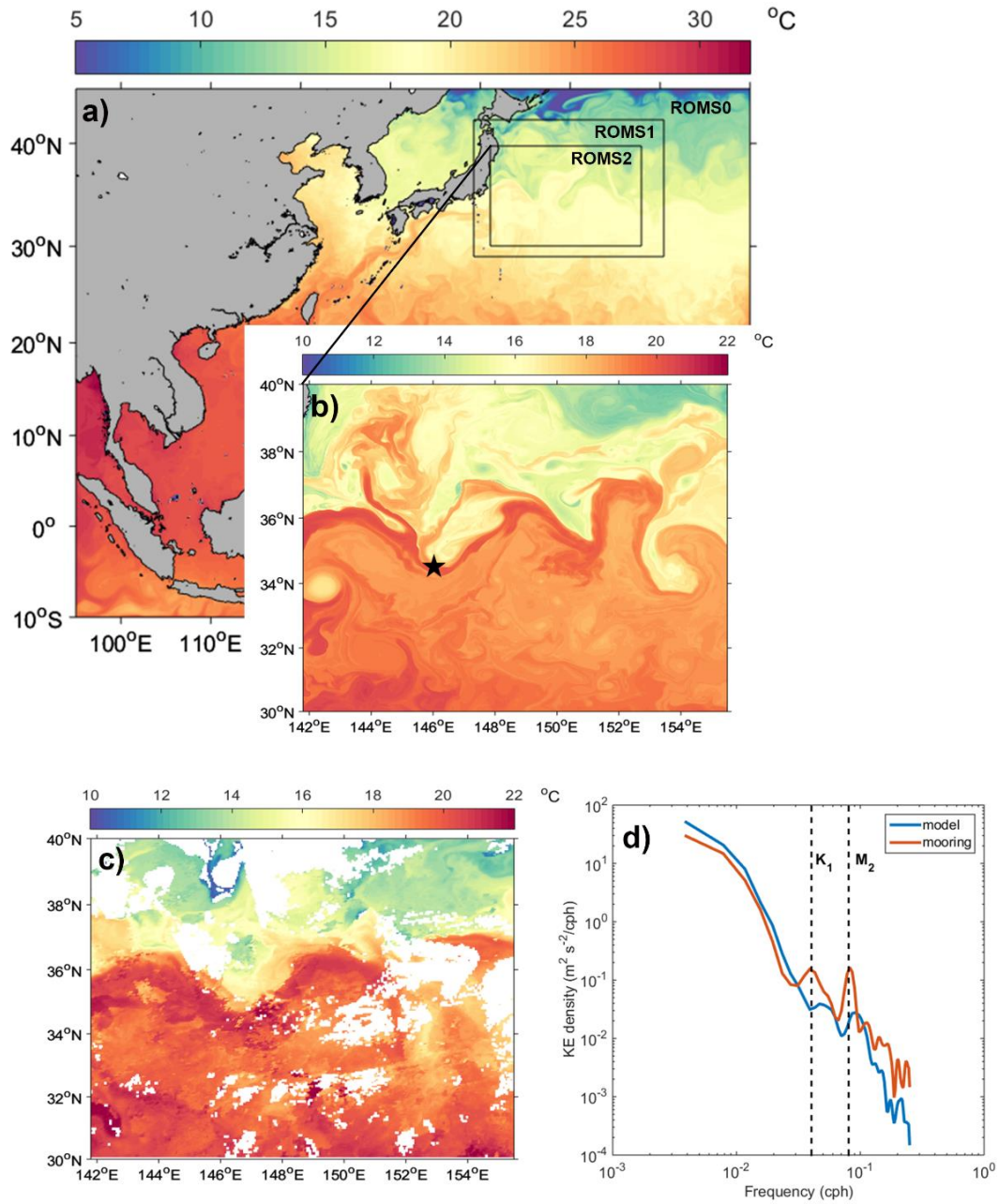
933 Waterman, S, N. Hogg, and S. Jayne, 2011: Eddy-mean flow interaction in the Kuroshio

934 Extension region. *J. Phys. Oceanogr.*, **41**, 1182–1208,

935 <http://doi.org/10.1175/2010JPO4564.1>.

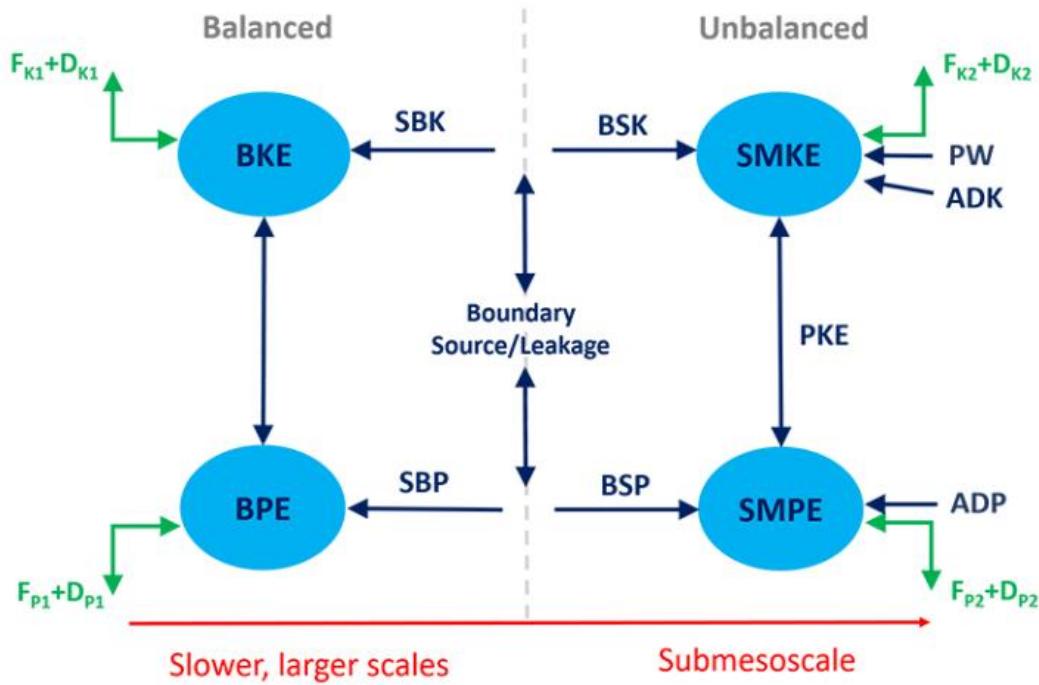
936 Woodruff, S., S. Worley, S. Lubker, Z. Ji, J. Eric Freeman, D. Berry, P. Brohan, E. Kent, R.  
937 Reynolds, S. Smith, and C. Wilkinson, 2011: ICOADS Release 2.5: extensions and  
938 enhancements to the surface marine meteorological archive. *Int. J. Climatol.*, **31**, 951–967,  
939 <https://doi.org/10.1002/joc.2103>.

940 Yan, X., D. Kang, E. N. Curchitser, and C. Pang, 2019: Energetics of eddy-mean flow  
941 interactions along the western boundary currents in the North Pacific. *J. Phys. Oceanogr.*,  
942 **49**, 789–810, <https://doi.org/10.1175/JPO-D-18-0201.1>.



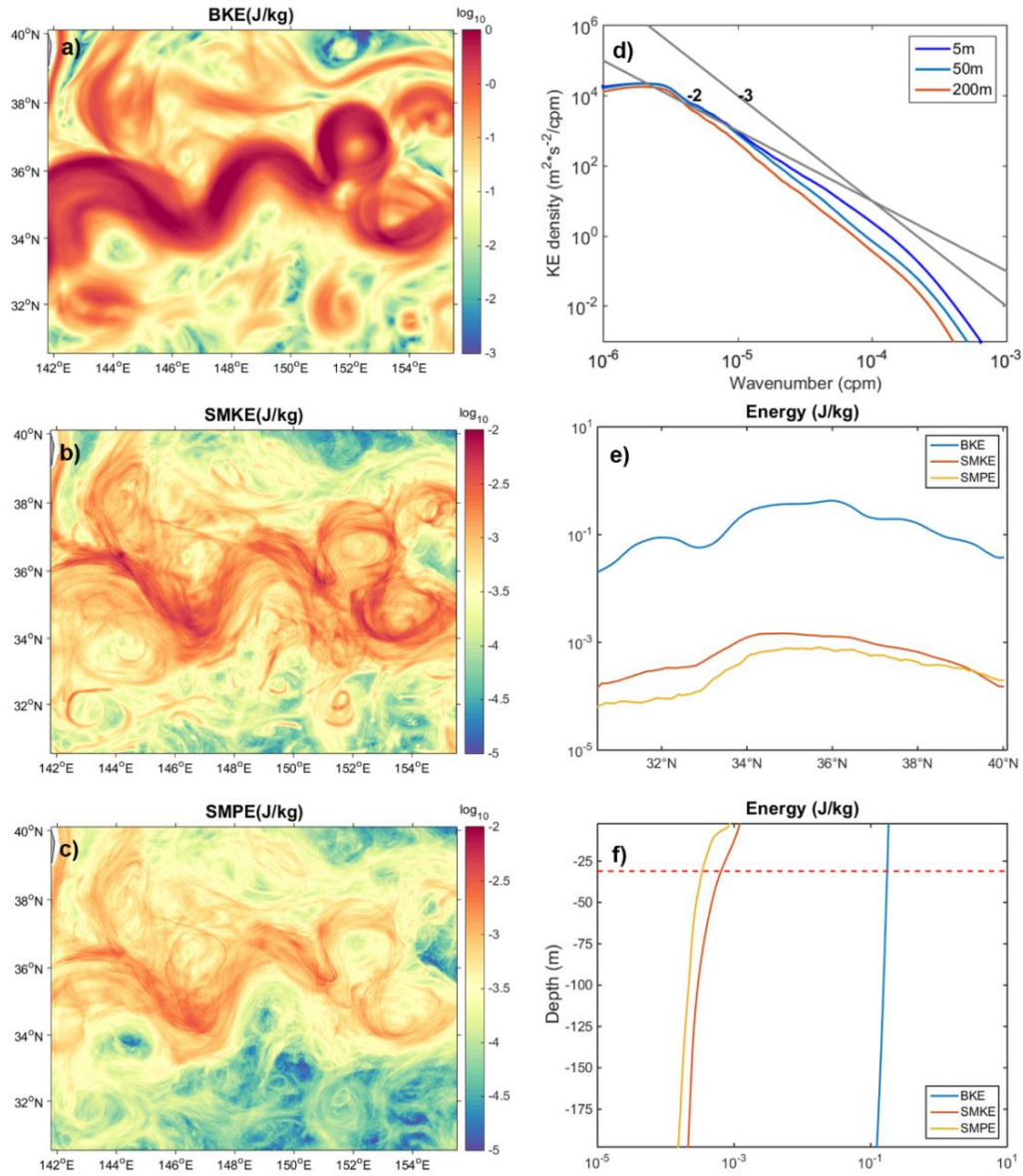
944

945 FIG.1. (a) Model surface temperature in domains of nested models at horizontal resolutions  
 946 of  $\sim 7.5$  km (ROMS0),  $\sim 1.5$  km (ROMS1), and  $\sim 0.5$  km (ROMS2) respectively. (b) The  
 947 simulated sea surface temperature compared with (c) that from MODIS-Aqua on May 1,  
 948 2018. (d) The comparison of the upper-ocean (50–200 m) velocity spectra between the model  
 949 and the KESS mooring at  $146.0^\circ\text{E}$ ,  $34.5^\circ\text{N}$  (black star in b).

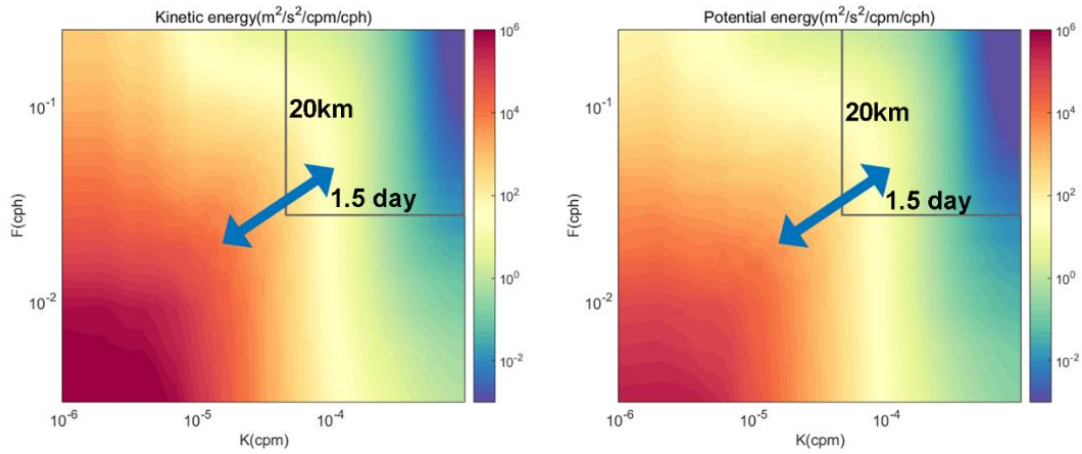


950

951 FIG. 2. Diagram of Lorenz (1955) energy cycle as evaluated between background scales (all  
 952 non-submesoscales) and submesoscales (scales smaller than 20 km and faster than 1.5 days).  
 953 Four energy reservoirs are defined as background kinetic energy (BKE), background  
 954 potential energy (BPE), submesoscale kinetic energy (SMKE), and submesoscale potential  
 955 energy (SMPE). BSK is the KE transfer from the background scales and submesoscale.  
 956 Likewise, BSP is the PE transfer from the background and submesoscale. PKE represents the  
 957 energy release of submesoscale available potential energy via buoyancy production,  
 958 indicating baroclinic instability pathways. PW, ADK, and ADP represent the pressure work,  
 959 advection effects on kinetic and potential energy respectively. Note that additional boundary  
 960 terms of energy leakage/source representing the energy from (to) outer domains are required  
 961 for the energetic analysis in regional seas. The sum of SBK and BSK (SBP and BSK) is  
 962 expected to be zero when there is no boundary leakage/source for KE (PE). The green arrows  
 963 denote the combined effects of atmosphere forcing ( $F_K$  and  $F_P$ ) and dissipation ( $D_K$  and  $D_P$ ).



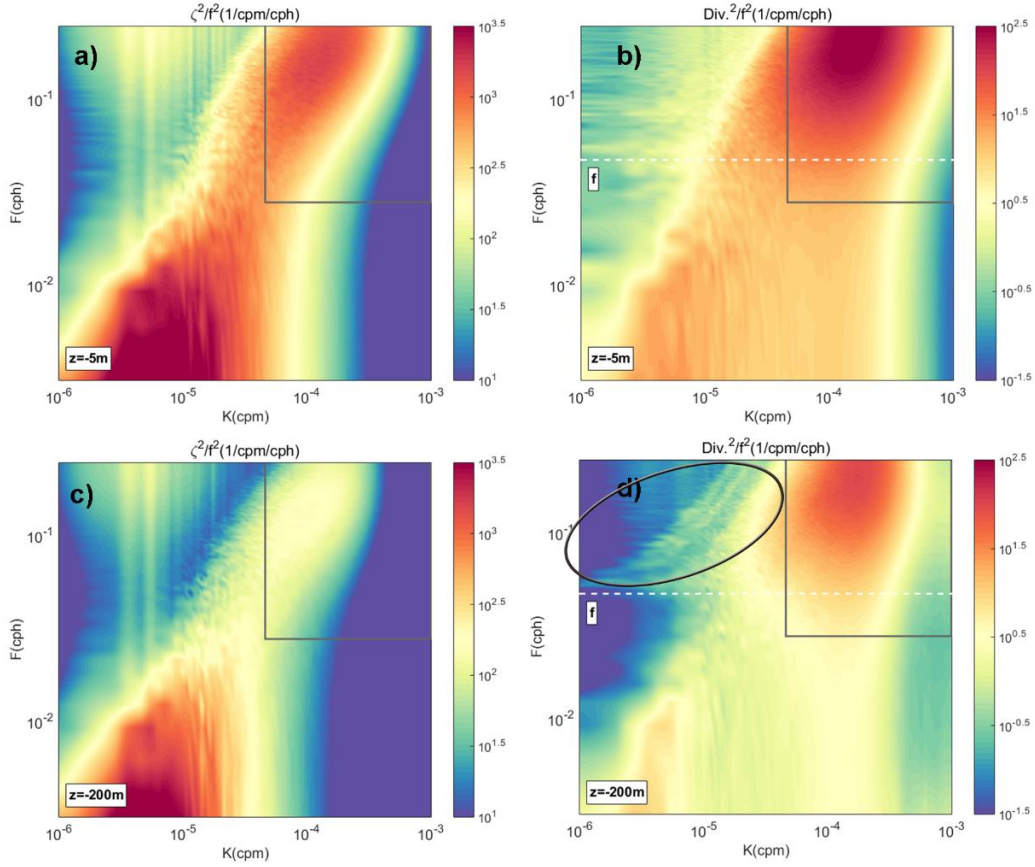
964  
 965 FIG. 3. Maps of averaged energy level of (a) BKE, (b) SMKE, and (c) SMPE. (d) The  
 966 wavenumber spectrum of KE. The  $-2$  and  $-3$  power line are plotted for reference. (e) The  
 967 zonally-averaged BKE, SMKE, and SMPE. (f) The vertical profile of the three energy terms.  
 968 The read dashed line denotes the averaged mixed layer depth.



969

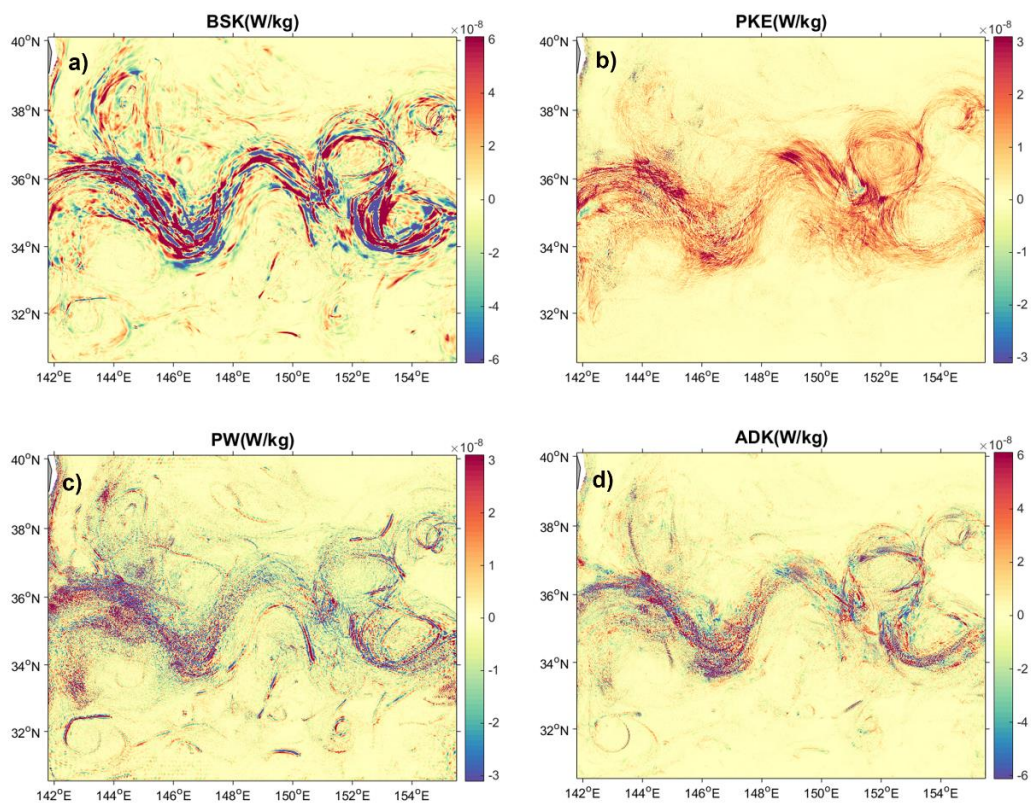
970 FIG. 4. Frequency–wavenumber spectra of kinetic and potential energy at  $z = -5$  m. The  
 971 submesoscale is marked by the grey-line rectangle boxes and the double arrows denote the  
 972 energy transfer between different scales.





973

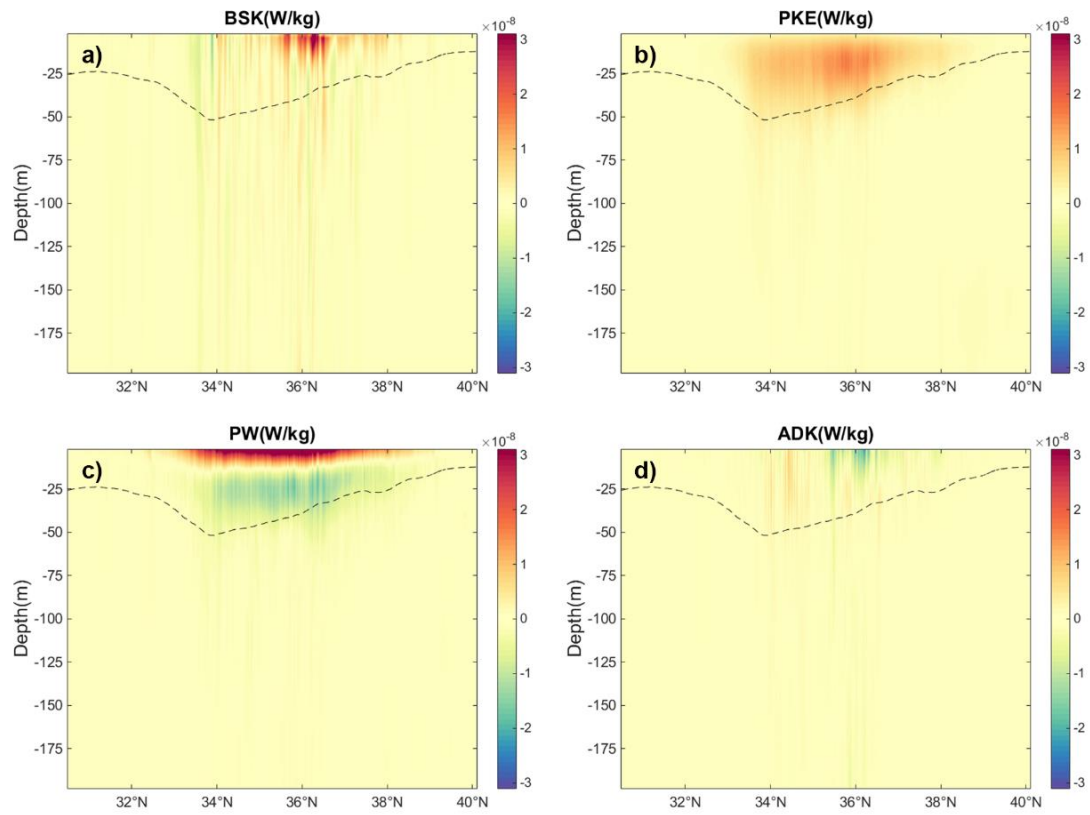
974 FIG. 5. Frequency–wavenumber spectra of (a),(c) vertical vorticity and (b),(d) horizontal  
 975 divergence at  $z = -5$  m and  $z = -200$  m, respectively. The submesoscale is marked by the  
 976 grey-line rectangle boxes and the inertial gravity wave band is marked by the ellipse. The  
 977 black dashed lines in (b) and (d) indicate the inertial frequency.



978

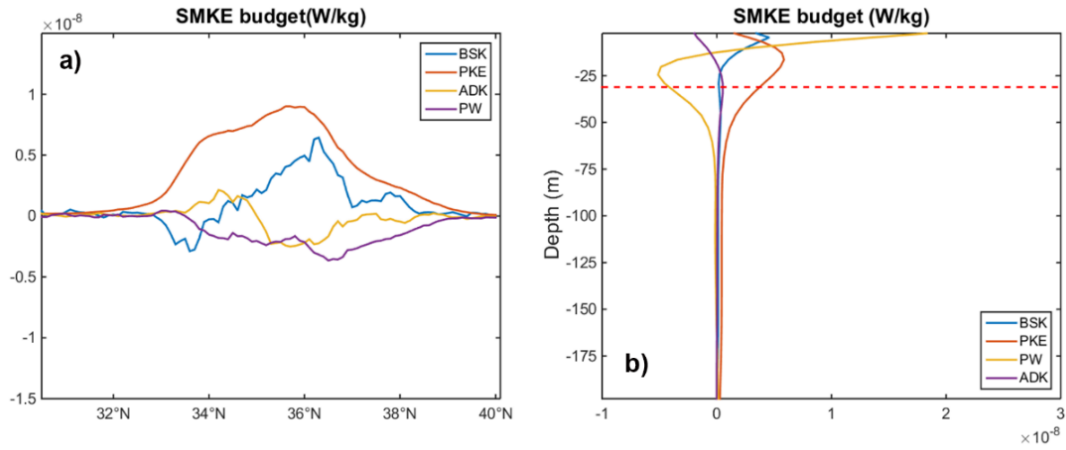
979 FIG. 6. Horizontal distribution of (a) BSK, (b) PKE, (c) PW and (d) ADK averaged over the  
980 upper 50 m.

981



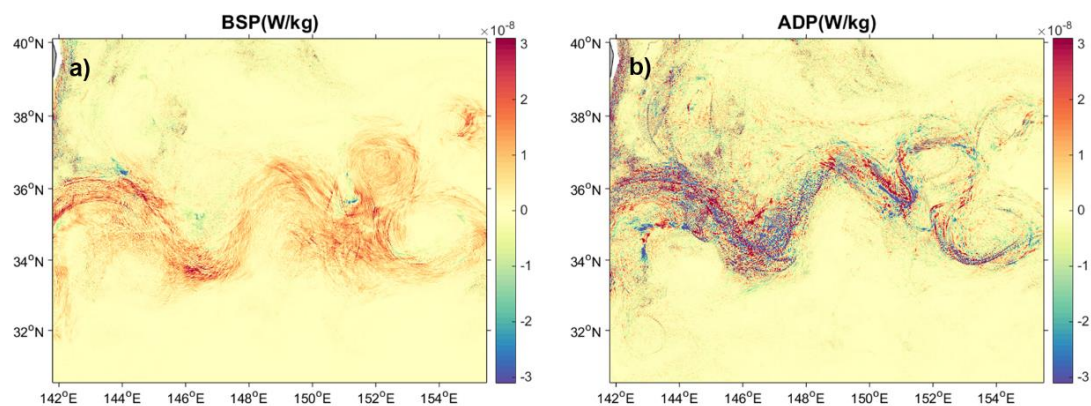
982

983 FIG. 7. Zonal-mean latitude-depth sections of (a) BSK, (b) PKE, (c) PW and (d) ADK. The  
 984 black dashed lines denote the zonally averaged mixed layer depth.



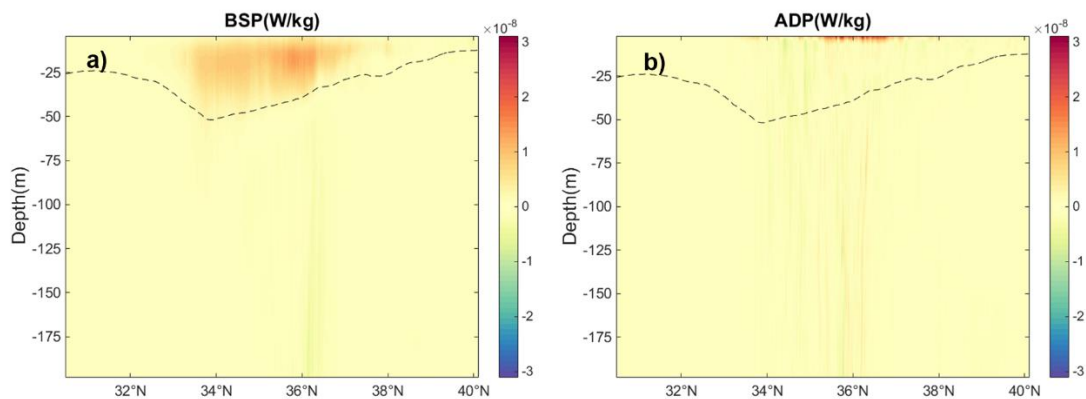
985

986 FIG. 8. (a) Vertically- and zonally-averaged, latitude-dependent plots and (b) horizontally-  
 987 averaged vertical profiles of SMKE production terms. The red dashed line denotes the  
 988 averaged mixed layer depth of the whole research domain.



989

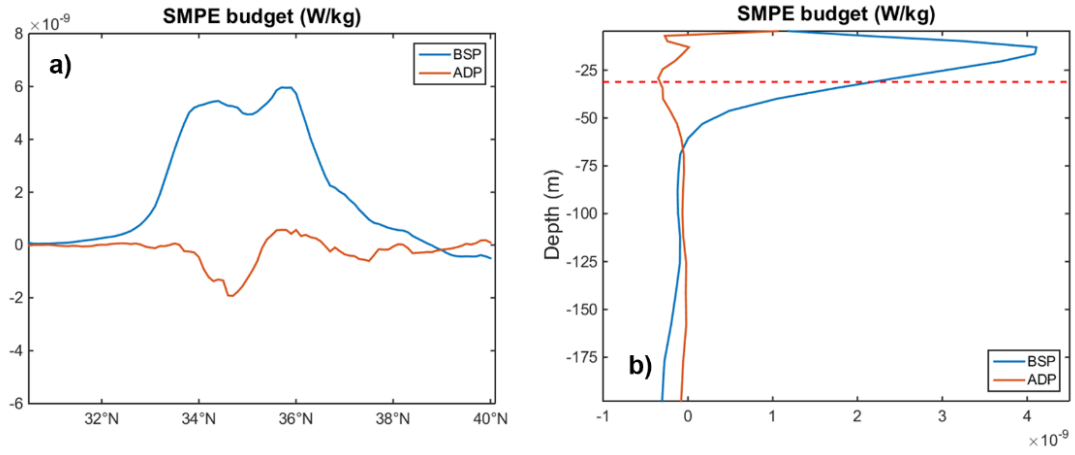
990 FIG. 9. Horizontal distribution of (a)BSP and (b) ADP averaged over the upper 50 m.



991

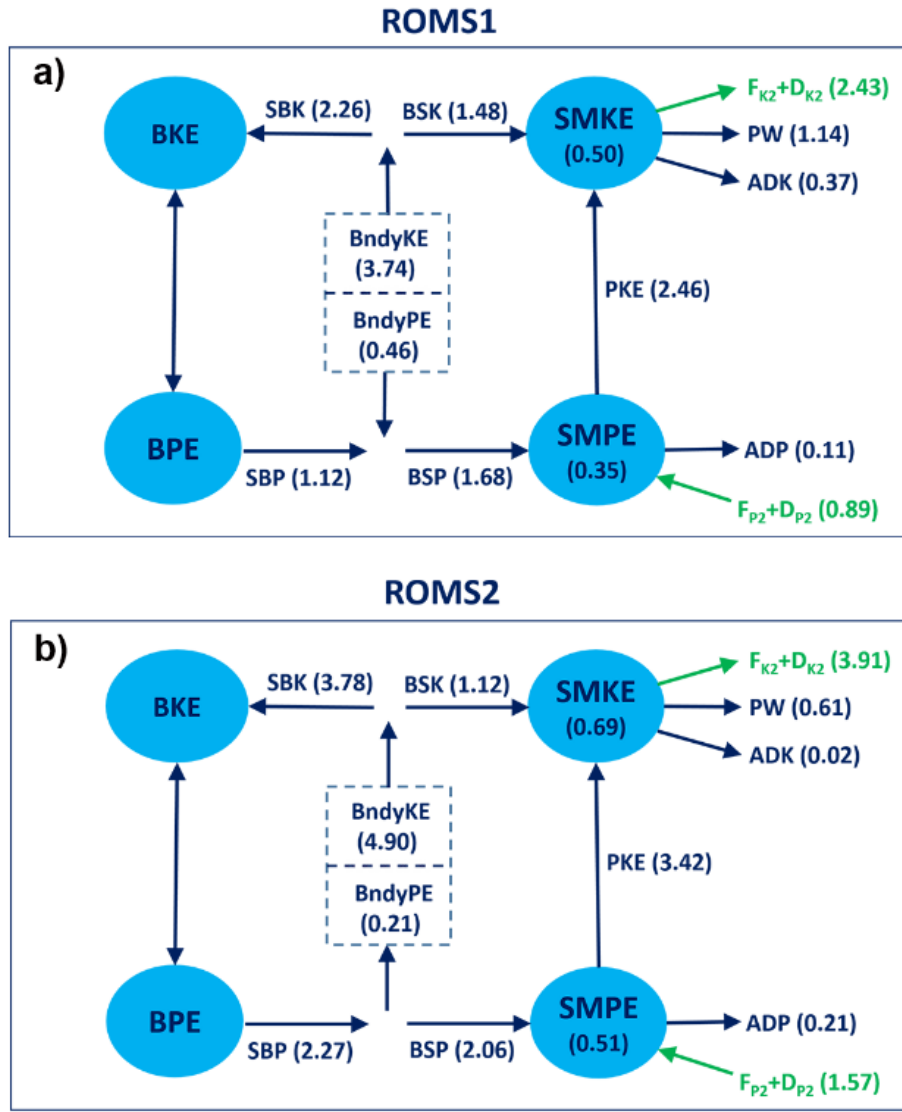
992 FIG. 10. Zonal-mean, vertical section plots of (a) BSP and (b) ADP. The black dashed line  
 993 denotes the zonally averaged mixed layer depth.

994



995

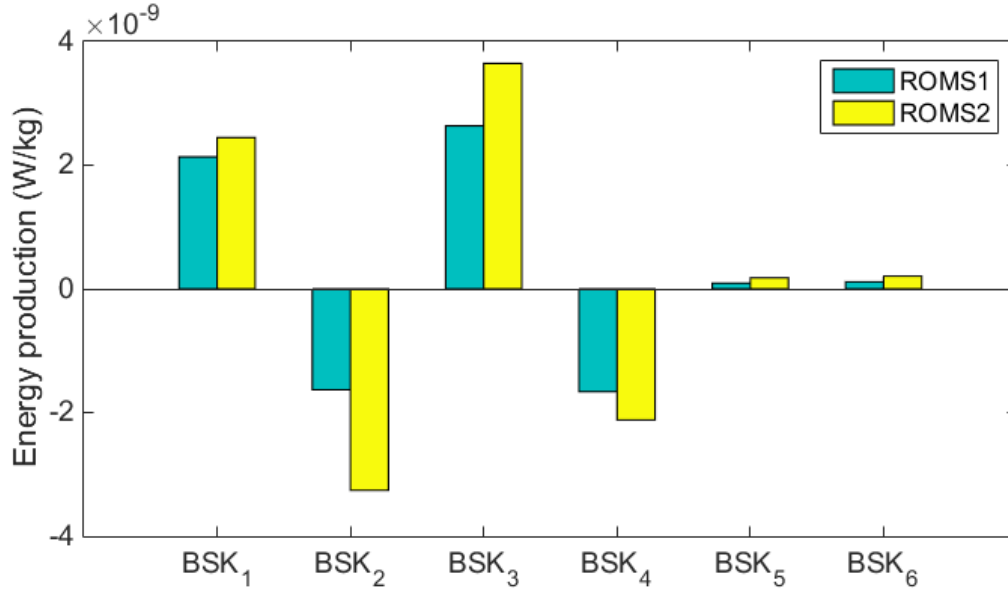
996 FIG. 11. (a) Vertically- and zonally-averaged, latitude-dependent plot and (b) horizontally-  
 997 averaged vertical profiles of SMPE production terms. The red dashed line denotes the  
 998 averaged mixed layer depth of the whole research domain.



999

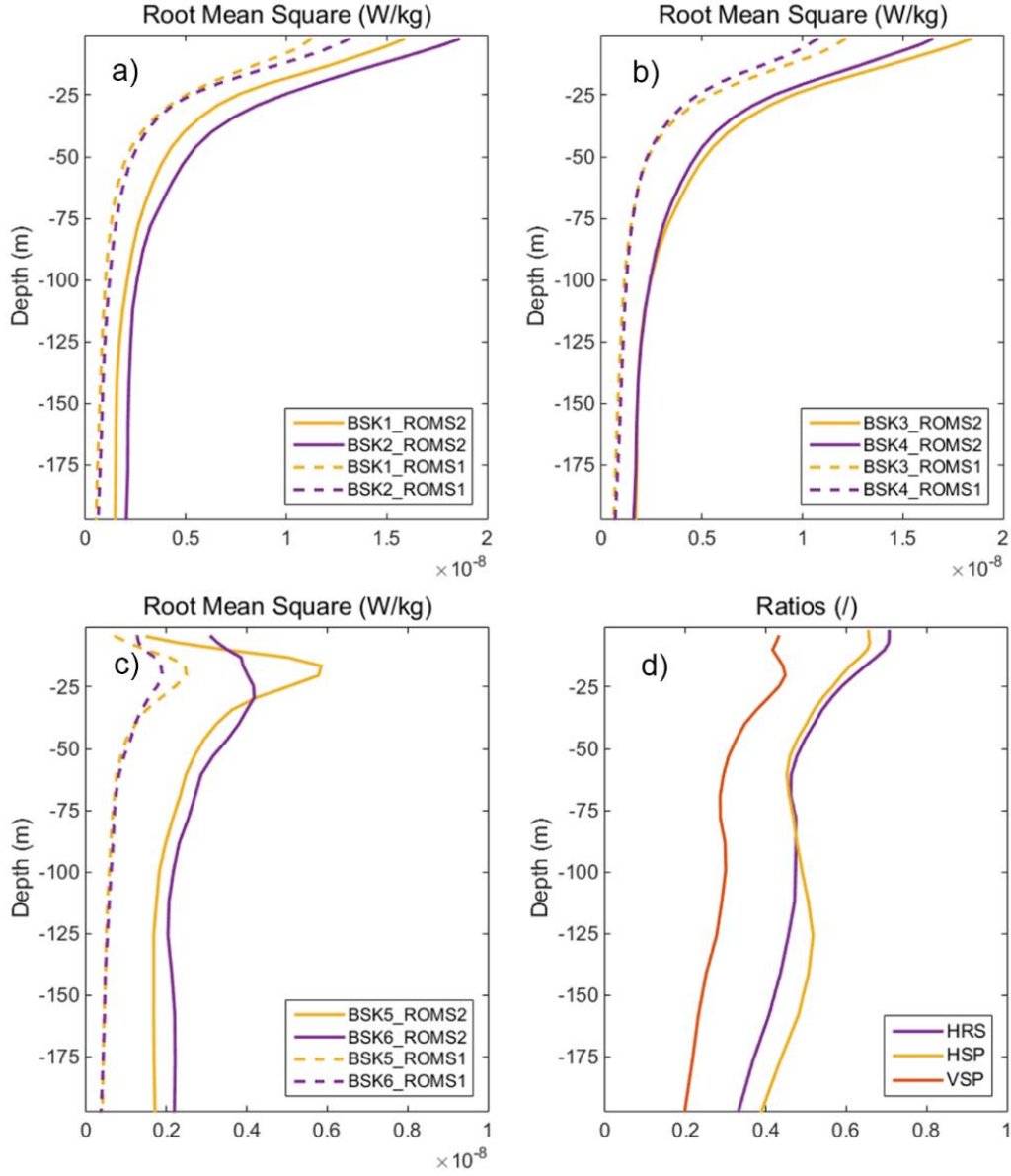
1000 FIG. 12. Schematics of averaged energy conversion rates for ROMS1 and ROMS2 in units of  
 1001  $10^{-9}$  W/kg and the energy reservoir in units of  $10^{-3}$  J/kg. Compared to Figure 2, the arrows  
 1002 illustrate the direction of energy transfers and energy leakage or source for boundary KE and  
 1003 PE. Note that the green arrows denote the combined effects of forcing and dissipation at the  
 1004 submesoscale when the SMKE and SMPE are assumed to be constant during the period  
 1005 ( $\partial \text{SMKE} / \partial t = 0$  and  $\partial \text{SMPE} / \partial t = 0$ ).





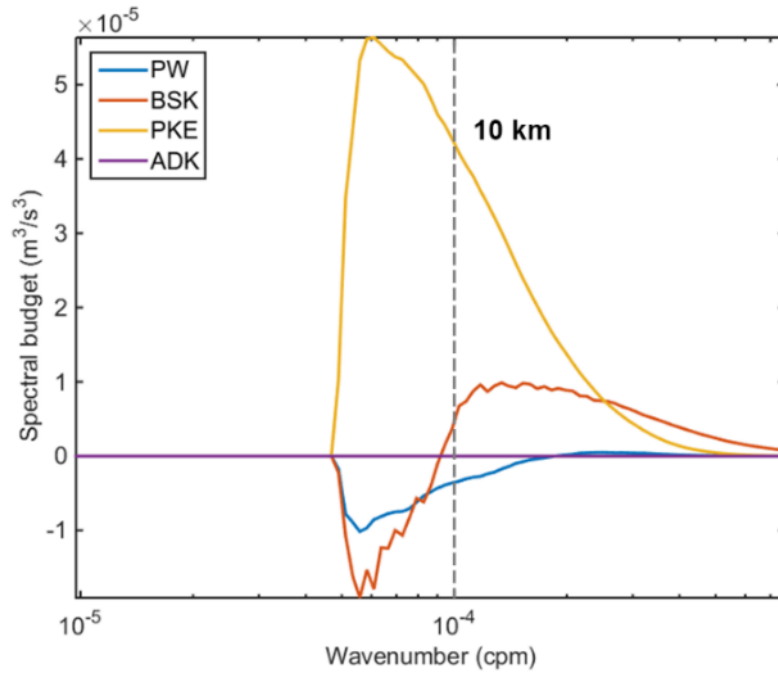
1006

1007 Fig. 13. Decomposed shear production (BSK) components averaged over the upper 50 m.  
 1008 The light blue bars are the ROMS1 simulation and yellow bars are the ROMS2 simulation.  
 1009 BSK<sub>1</sub> and BSK<sub>2</sub> denote energy production by normal horizontal Reynolds stresses (HRS);  
 1010 BSK<sub>3</sub> and BSK<sub>4</sub> denote horizontal shear production by torsional stresses (HSP); BSK<sub>5</sub> and  
 1011 BSK<sub>6</sub> denote vertical shear production (VSP).



1012

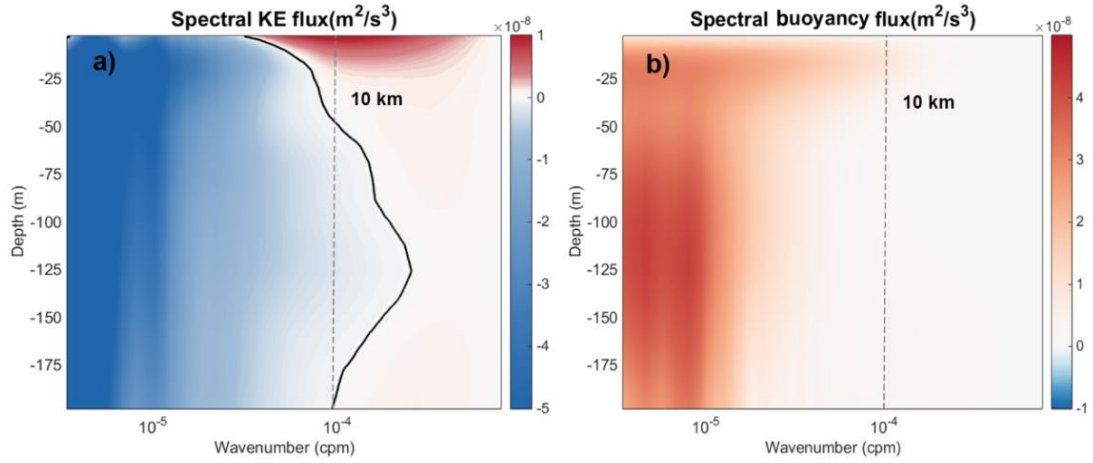
1013 FIG. 14. Vertical profiles of root-mean-square values of (a) BSK1 and BSK2 (production by  
 1014 normal horizontal Reynolds stress: HRS), (b) BSK3 and BSK4 (horizontal shear production  
 1015 by torsional stresses), and (c) BSK5 and BSK6 (vertical shear production) for the ROMS1  
 1016 and ROMS2 simulation in the research domain. (d) Ratios between ROMS1 and ROMS2  
 1017 simulation for HRS, HSP, and VSP.



1018

1019 FIG. 15. Spectral pressure work (PW), background to submesoscale kinetic energy  
 1020 production (BSK), submesoscale potential to kinetic energy transfers (PKE), and advection of  
 1021 submesoscale kinetic energy (ADK) averaged over the upper 50 m. The dashed line indicates  
 1022 the wavelength of 10 km.

1023



1024

1025 FIG. 16. Depth-scale plots of (a) KE flux and (b) buoyancy flux. The shading in blue denotes  
 1026 negative flux (energy transfer to larger scales) and the red shading means positive flux  
 1027 (energy transfer to smaller scales). The black solid line denotes the transition from negative  
 1028 to positive KE flux ( $\Pi(k) = 0$ ). The dashed lines indicate the wavelength of 10 km.